The influence of morphology and the loading-unloading process on discontinuity stress states observed via photoelastic technique and its inspiration to induced seismicity

Dapeng Wang [a,b], Jianchun Li [b,**], Chunjiang Zou [c,*], Zhijie Wang [b], Jian Zhao [a]

[a] Department of Civil Engineering, Monash University, Clayton, Australia
[b] School of Civil Engineering, Institute of Future Underground Space, Southeast University, Nanjing, China
[c] Department of Civil Engineering, Brunel University, London, United Kingdom

ABSTRACT

Stress change in rock mass caused by human activities has the potential to cause the sliding and destruction of faults and joints, resulting in induced seismicity. Laboratory experiments are conducted on a simulated fault with various teeth numbers and undulation angles to uncover the mechanism of stress change-induced seismicity. The potential risk of induced seismicity is explained using three methods: the Mohr-Coulomb failure criterion, localization of stress concentration regions, and visualization of maximum shear stress reduction through photoelasticity. Experimental results indicate that the friction coefficient increases with the undulation angle, and the form of stress change has an unignorable impact on frictional instability. The friction coefficient in the vertical unloading process is slightly lower than that in the loading process and larger than that in the shear unloading process. Loading is the stress change caused by shear displacement under constant normal stiffness conditions and unloading is the process of reducing the stress by controlling the position of the boundary constraints in the corresponding direction. Meanwhile, unloading in the shear direction has both seismic and aseismic features. Although the rapid drop of shear stress at the onset of shear unloading may induce fault instability, the reduction of normal stress and the restoration of displacement prove that unloading in the shear direction may also reduce the risk of fault failure in the subsequent process. In addition, the stress concentration region is mainly distributed perpendicular to the contact surface rather than the entire fault. This research is conducive to promoting the application of photoelasticity in studying induced seismicity and provides a practical method for calculating the energy released during such events. Based on the morphological characteristics and stress states of fault surfaces, the findings can be utilized in engineering practice to assess the risk of induced seismicity under different stress change conditions.

List of symbols

L	total joint length	nJRC	Nominal joint roughness coefficient
α	undulation angle	E	Young's modulus
σ	compressive strength	ρ	density
c	phase velocity	ν	Poisson ratio
f_d	material fringe constant in N/mm/fringe	N	photoelastic fringe order
ΔN	extinction fringe order	H	thickness of the sample
$F_{N \text{ initial}}$	initial normal force	A	fault area

(continued on next column)

(continued)

F_S	shear force measured by the sensor	F_N	normal force measured by the sensor
F_S^1	resolved shear force	F_N^1	resolved normal force
τ_{max}	maximum shear stress	φ_0	the friction angle of a flat and straight joint
S_d	shear displacement	$\sigma_1, \sigma_2, \sigma_3$	the first, second, third principal stresses
σ_V	vertical stress	σ_H	horizontal stress
$\Delta\sigma_N$	attenuation of surface normal stress	$\sigma_{N \text{ initial}}$	initial normal stress

(continued on next page)

* Corresponding author.
** Corresponding author.
  E-mail addresses: jcli@seu.edu.cn (J. Li), chunjiang.zou@brunel.ac.uk (C. Zou).

(*continued*)

E_s	total radiated seismic energy	r_a	apparent stress
Δd	incremental fault slip	M_w	moment magnitude
$\mu_0, \mu_1,$	the friction coefficient in the loading, unloading in the shear direction and		
μ_2	unloading in the vertical direction		
μ_r	the resolved friction coefficient		

1. Introduction

Induced seismicity is earthquakes caused by human activities, generally of a low magnitude. The root cause of induced seismicity is that engineering activities break the original equilibrium state of the underground stress field, and the process of seeking to rebalance induces structure failure. Human activities that cause induced earthquakes include wastewater injection,[1–3] withdrawal of gas and fluid from the subsurface,[4,5] mining projects,[6,7] reservoir impoundment,[8,9] and geothermal energy extraction.[10,11]

Despite the enormous economic potential of exploring and utilizing underground space resources,[12–15] numerous governments have set limits on the magnitude of the induced seismicity to protect the lives of residents and reduce panic. Production and operation of the existing project will cease when the magnitude exceeds the limiting value. The local government stopped the enhanced geothermal system (EGS) in Basel, Switzerland, due to the felt seismic events.[16] Häring et al.[17] took micro-seismic events as an inherent feature within current reservoir stimulation and tried to analyze the possible mechanism of the shearing process. A magnitude 5.4 seismic event was reported in Pohang City, Korea.[18,19] Researchers explained that this shallow-depth earthquake was induced by a local EGS project. Although some researchers[20] considered this event to be either a natural or triggered, but not an induced seismic event, this project has been stopped by the local government, and the restart time is still uncertain. Induced seismicity can also cause geo-hazards like rock avalanches, surface subsidence, landside-dammed lakes and debris flows, which will lead to ecosystem degradation and vegetation destruction.[21–23]

Due to the impact of induced earthquakes on human activities and the environment, dealing with induced seismicity has become a worldwide concern. Researchers make comprehensive reviews[24–29] on chains and mechanisms of induced seismicity. The recognized mechanisms of induced seismicity include modifying the pore pressure and/or stress, earthquake nucleation, and changes in friction coefficient. Extensive research[30–35] is conducted based on these mechanisms or to explore other possibilities. With significant advancements in the application of new experimental apparatus and simulation techniques, researchers are getting closer to cracking the mechanism of stress change-induced seismicity. Wu[36] reviewed unloading-induced seismicity caused by developing underground space and extracting underground sources and summarized some unusual cases that the Mohr-Coulomb failure criterion cannot explain. Kang et al.[25] explained the fault slip caused by quarry unloading and reservoir impoundment with Mohr circles. Wu et al.[37] hold that induced earthquakes happen when human activities perturb the frictional equilibrium of pre-existing faults. Mining activities could cause stress redistribution and induce fault slip. Excavation of underground mineral resources could change the stress and cause fracture initiation or fault slip adjacent to the orebody. Sainoki and Mitri[38] simulated mining-induced fault slip with Flac-3D. They concluded that the friction angle and location of the fault are critical factors, while the dilation angle and stiffness do not have much effect. The fault slip caused by excavation was considered a prominent type of rock burst.[39] The fault slip burst was defined as a rock burst caused by the movement of the pre-existing fault or the formation of earthquake-prone structural zones.[40] The frictional properties of faults greatly influence induced seismicity caused by stress change and depend on the blocks' structural characteristics, physical properties, and the filling material as fault gauge or fluid between them.[41–44] The direction, magnitude, and evolution of the maximum compressive stress in the tectonic stress field also significantly impacted the friction property of the fault.[45] The water lubrication effect was experimentally studied, and the result found that the fault in wet conditions has a lower friction coefficient, which reduces both adhesive force and shear stress.[46] However, the process of stress redistribution which causes fault instability remains unclear. Li et al.[47] used a biaxial Hopkinson pressure bar to study the shear behavior of sawtooth-shaped rock joints. The influence of environment and temperature is also becoming an influential subject.

Although many studies have examined induced seismicity under various intrinsic structural characteristics and external loading conditions, few attempts have been conducted to observe the stress concentration regions and maximum shear stress variations along the fault directly, which generally control fault failure. Also, the boundary conditions for most experimental studies are limited to constant normal stress conditions, which are inconsistent with many engineering practices. This research aims to uncover the seismic response when stress conditions along the fault change and identify the factors that govern fault behavior. The frictional experiments are conducted using a custom direct shear machine that is combined with photoelasticity. The primary parameters considered to affect fault frictional behavior during stress change include the initial normal stress, shear displacement, unloading mode and fault morphology (undulation angle and teeth number). Based on the experimental results, the characteristics of induced seismicity caused by the change of initial stress state can be recognized, and the identification of the most hazardous regions is highly likely to be realized.

2. Experimental setup

2.1. Sample preparation

The fault surfaces in nature are generally irregular in shape with various numbers of convex and undulation angles. While laboratory experiments aim to replicate natural conditions as closely as possible, the irregular morphological parameters are simplified into different numbers of teeth with various undulation angles because every natural profile consists of various and large amounts of single teeth. Barton[48] proposed a joint roughness coefficient (JRC) to describe the surface roughness scaled from 0 to 20. Although the scale of the joints and faults vary, this research adopts the nominal JRC (nJRC) for surface morphological description to facilitate grouping and comparison. As JRC and nJRC are identical in values and calculation methods, JRC will continue to be used in all subsequent descriptions in this paper. The JRC is calculated by the revised Tse empirical formula[49]:

$$JRC = 32.69 + 32.98 \, lg \, Z_2 \tag{1}$$

$$Z_2 = \sqrt{\frac{1}{m(\Delta x)^2} \sum_{i=1}^{m} (y_{i+1} - y_i)^2} \tag{2}$$

In this equation, Z_2 is the root mean square of the first derivative of the profile, m is the number of sampling intervals, Δx is the sampling interval, y_{i+1} and y_i are the heights of the ith and i+1st sampling points, respectively. A sampling interval of less than 1 mm is sufficient to capture the micro-features of joint roughness.[50] In this study, Δx is set to 0.5 mm and m is 200. Thus, the JRC of the samples (Fig. 1) ranges from 9.6 to 19.1, which is the most widespread in the natural rock mass.[51]

Test specimens used in the experiments are made of polycarbonate with sensitive temporary birefringent properties, each consisting of two plates. As shown in Fig. 1, seven groups of polycarbonate cuboid specimens are prepared, including prefabricated fault with two teeth and different JRC (9.6, 11.2, 13.2, 16.2), fault with three teeth and different JRC (16.2 and 19.2), and a straight fault for reference. The dimension of the sample is 100 mm*100 mm*10 mm, and the corresponding undulation angle α is also listed. The two ends of the artificial fault are in the
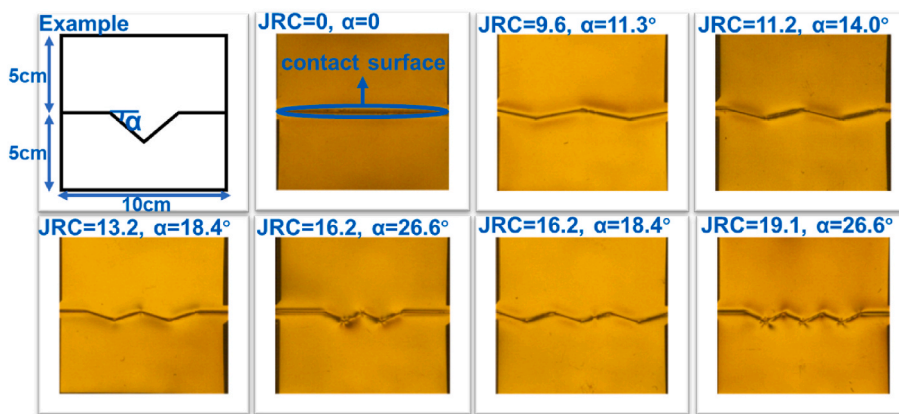
Fig. 1. Polycarbonate samples and relevant geometry parameters.

middle of opposite sides. Since the simulated fault surfaces in this experiment are composed of relatively simple polygonal shapes, the fracture surfaces are designed and machined using a lathe with a precision of 0.001 mm. This ensured smooth, well-fitted contact surfaces without significant protrusions. 3D printing technology has also been widely utilized in photoelastic experiments, particularly for joints with complex morphologies.[52,53] The samples are annealed to eliminate residual stress and avoid the stress concentration phenomenon when there is no external force. Additionally, Under external loading, the specimen should not fail due to asperities, and no residual stress should remain after unloading. Polishing or other measures that may cause material failure should be avoided. The basic physical and mechanical properties of polycarbonate specimens are listed in Table 1.

Where, E denotes Young's modulus, σ denotes the maximum compressive strength, ρ denotes the density, c denotes the phase velocity, and ν is the Poisson ratio. The f_d is the material fringe value in N/mm/fringe and will be described in detail in Chapter 2.3.

Finding model materials for photoelastic experiments that match the physical and mechanical properties of natural rock mass is a significant challenge. The polycarbonate material used in this experiment exhibits linear elastic deformation characteristics, making it suitable for quantitative photoelastic stress analysis. Although there are differences in mechanical properties such as plasticity, ductility, and fracture toughness compared to natural rock mass, the model offers distinct advantages in terms of internal structure transparency, stress field visualization, and experimental reproducibility. We are also exploring material modification methods to enhance the mechanical similarity between experimental materials and natural rock mass. For example, we are exploring the possibility of using 3D printing technology with different chemical compositions of printing materials, as well as randomly introducing micro-pores and micro-cracks,[52–54] which are believed to have the potential to better simulate typical jointed rock masses.

2.2. Test setup

This test system (Fig. 2a) combines a photoelastic apparatus and a customized direct shear machine. The photoelastic apparatus (TST-300[55,56]) contains an orange laser light source (600 nm wavelength), a laser power adapter, two metal guide rails, a collimating lens, a polarizer, an analyzer, a field lens, and a high-speed camera (phantom V2512). The metal guide rails (Fig. 2b) are customed to ensure the

continuity of the optical path and the stability of the test. The specimen is fixed on the plane perpendicular to the laser incidence direction, and the front view is shown in Fig. 2c. It must be ensured that the light source can pass through all devices completely and is not blocked. The experimental materials used for photoelasticity generally have low strength and can only be tested under low-loading conditions. The existing direct shear apparatus for rock tests is with low accuracy under low-stress conditions. Thus, this research designs a new direct shear machine for photoelastic experiments. As shown in Fig. 2d, the servo control shear apparatus is equipped with two force sensors and grating rulers on normal and shear directions for displacement and force measurement. The loading velocity in both directions can be set from 0 to 10 mm/s, and the maximum value for the loading force ranges from 0 to 14 kN. The sample fixing device (Fig. 2e) consists of the upper and lower shear boxes. The shear box has no cover in front and back so that the high-speed camera can record the deformation and sliding process of specimens. Grooves are prefabricated inside of the shear box to ensure that the sample will not mismove or slip during the test.

2.3. The principle of the photoelastic method

Photoelastic analysis is commonly used to study systems with complex boundaries, such as underground excavations with irregular shapes. Photographs of isochromatic, along with calculated stress trajectories, provide valuable insights into the stress distribution and highlight areas of stress concentration.[57] Photoelastic stress analysis experiments are also conducted to validate the accuracy of the stress contours produced by the numerical method.[58–60] Photoelastic techniques have been widely used for transparent materials. In rock mechanic research, the photoelastic method has an irreplaceable advantage in visualizing stress concentration.[61,62] The influence of joints on the stress field with dynamic is investigated photoelastic equipment.[63] Although numerical simulations are very powerful, many experimental conditions cannot be fully represented due to technical limitations and photoelastic research cannot be completely replaced by numerical simulations for detailed studies. For example, the setting of contact characteristics is relatively simplistic in numerical simulations, whereas in actual research, the characteristics of the contact surface change during the shearing process, which cannot be captured in simulations. Additionally, the increase in local stress may lead to changes in the mechanical properties of the local material. In numerical simulations, materials are usually set as homogeneous and do not account for changes observed during the experimental process. The combination of photoelasticity and high-speed cameras allows for detailed observation of the failure process, which would require significant time and computational resources in numerical simulations. Photoelastic experiments provide a critical bridge between laboratory rock testing and numerical simulation. By conducting experiments using photoelastic
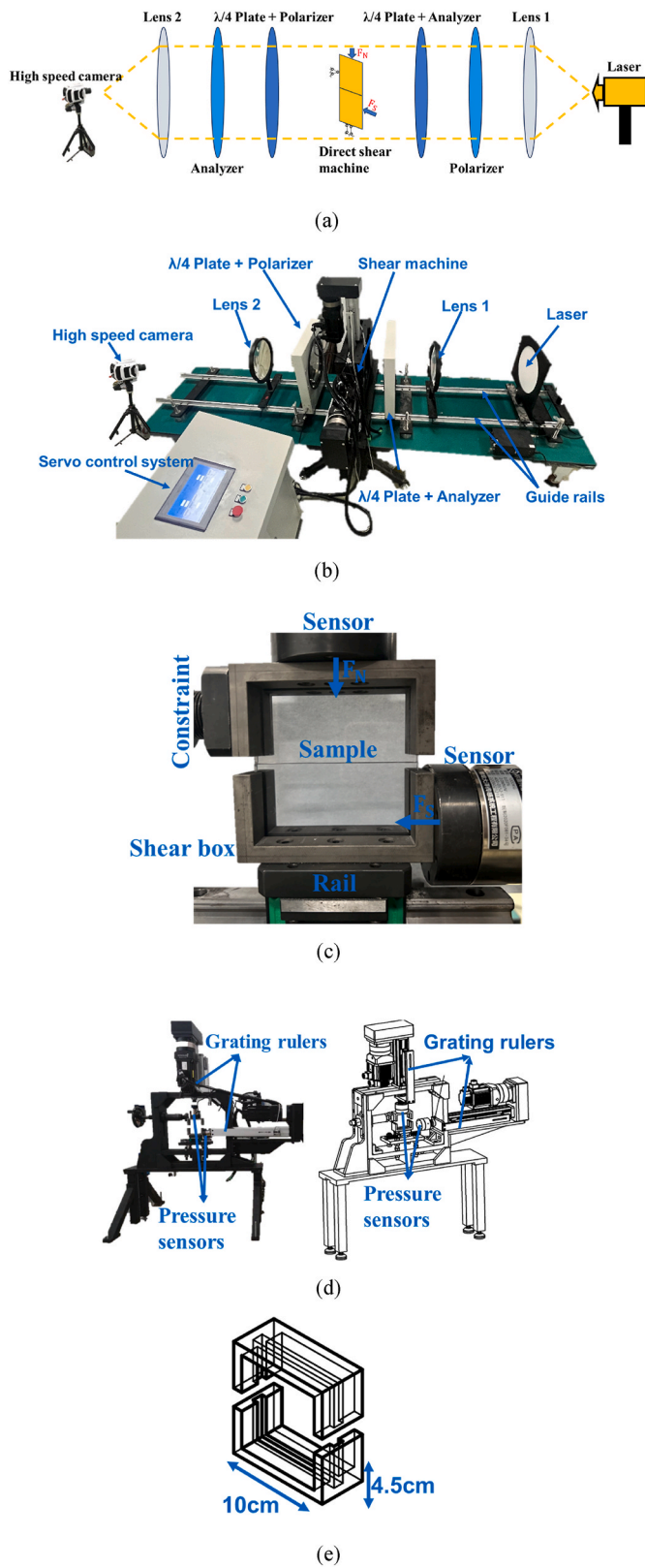
Table 1
Mechanic properties of polycarbonate specimens.

E	σ	ρ	c	ν	f_d
2.1 GPa	78 MPa	1690 kg/m3	1033 m/s	0.28	7.466 N/mm/fringe

(a)

(b)

(c)

(d)

(e)

Fig. 2. (a) Schematics of the photoelastic testing system, (b) photo of the experimental apparatus, and (c) front view of the loading device. (d) Photo and schematic of the customed direct shear machine for photoelastic experiment and (e) geometry of the shear box.

stress analysis, researchers can compare the shape of the maximum shear stress contours obtained from these experiments with those derived from numerical methods.[58,59] Thus, the photoelastic experiment plays an important role in insuring that the stress contours produced by the numerical method are correct. In addition, the method of mesh division in numerical simulations is crucial for improving the accuracy of energy calculations in photoelastic tests. Specifically, this can be achieved by increasing the grid density in stress concentration regions and reducing it in other areas.

The fringes caused by elastic deformation in the sample are proportional to the internal shear stress field. The temporary birefringent property of polycarbonate material enables us to observe and calculate the stress concentration region around the fault. The stress concentration phenomenon becomes more obvious with higher fringe order. In photoelastic analysis, light-field and dark-field isochromatic fringe patterns are obtained to calculate the half-order and whole-order fringe. In this research, the polarizer and analyzer are rotated to 45 and 315° to form a dark field, which means the fringe orders are N = 0, 1, 2, and n. The fringe order can be determined by the continuous loading method. The first step is to choose a standard point in the model; the load then increases from 0 to the rated value. Observing the extinction order on this point and the fringe order can determine the order of other fringes, which can then be calculated. The linear difference method will be adopted to obtain the approximated intermediate fringe order for the concerned points that are not exactly on the fringe. The stresses and optical property satisfy the relation:

$$\sigma_1 - \sigma_2 = \frac{Nf_d}{h} \quad (3)$$

where σ_1 and σ_2 denote the two main principal stresses, N denotes the fringe order, f_d denotes the material fringe value in N/mm/fringe, and h is the thickness of the sample (h = 10 mm in this case).

The value of f_d is determined by the disk radial compression test. The stress state at the center of the disk sample is shown in Fig. 3a. Based on elastic mechanics, the stress in the center is:

$$\sigma_1 = \frac{2P}{\pi dD} \quad (4)$$

$$\sigma_2 = \frac{-6P}{\pi dD} \quad (5)$$

Where P denotes normal pressure, D is the thickness of the disk. Then, the value of f_d can be determined by:

$$f_d = \frac{8P}{\pi DN} \quad (6)$$

According to the fringe order determination method described in the beginning, the fringe order in the center can be counted (Fig. 3b). Thus,
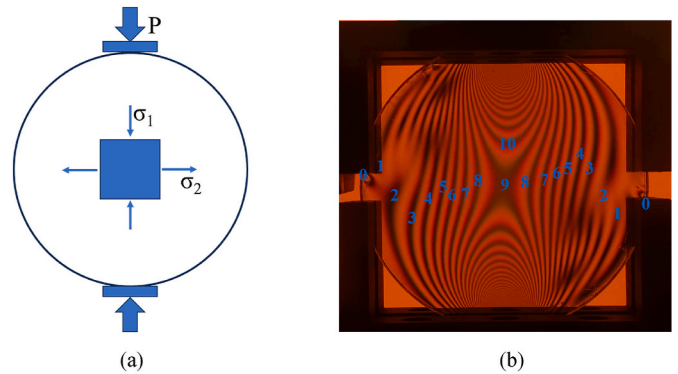

(a)

(b)

Fig. 3. Determination of material fringe constant in the photoelastic experiment (a) schematic of the stress state of the disk subjected to normal pressure and (b) photo of fringe order in a dark field.

f_d = 7.466 N/mm/fringe in this research.

2.4. Test procedure

As shown in Fig. 1, the samples are annealed to eliminate residual stress, and no fringe exists without external force. The samples are then fixed into the shear box through prefabricated grooves separately. Before taking the photoelastic experiment, all the optical apparatuses are fixed on the metal guide rails. The polarizer and analyzer are rotated to generate a dark-field polarized light.

During the loading test, the servo-controlled force sensor first applies an initial normal force ($F_{N\ initial}$). In this process, the normal load continuously increases at a constant rate until the specified normal force is attained. The initial normal stress at the top of the specimen ($\sigma_{N\ initial}$) can be calculated because the contact surface is 10^{-3} m^2 (Fig. 2e). The normal and shear force sensors and shearing box (Fig. 2c) are designed to ensure that the normal and shear load are uniformly distributed over the discontinuity. The constraints in normal and shear direction are imposed on the specimen by the shear box and sensors. When the F_N initial reaches the target value, the displacement in the vertical direction is constrained, which means the experiments are under constant normal stiffness loading conditions (CNS). Then, the shear displacement (S_d) of the lower (driving) block in the horizontal direction increases at a constant rate of 1 mm/s. Given that the specimen remains in the elastic deformation state, the shear rate has limited influence on the photoelastic test when the constraints do not disappear suddenly. In fact, the authors conducted trials with different shear rates of 0.5, 0.75, and 1 mm/s during experiments, and the final stress state is only determined by the shear displacement. In this test, the different shear displacements are set to create varying initial stress states. If the shear displacement is too long, overly dense fringes will appear in the stress concentration region, making it extremely difficult to count fringe order. Conversely, if the shear displacement is too short, the total amount of effective mechanical and optical data will be limited, preventing a convincing analysis. After trial and error, loading distances of 2 mm and 4 mm are selected as the optimal choices. The first non-zero value measured by the shear force sensor is recorded as the starting point of loading. Different stress states formed by loading represent various stress fields that faults are located in and are the initial stress conditions for unloading experiments. For shear unloading cases, the position of constraint in the normal direction is fixed, and the constraint in the shear direction retreats at 1 mm/s. The shear unloading process stops when the shear force (F_S) equals 0. For the vertical unloading case, the position of constraint in the normal direction retreats at 1 mm/s, and the normal unloading process stops when the normal force (F_N) equals 0. The forces in normal and shear directions are measured by force sensors, and the sampling rate is 10 data points per second (FPS). The high-speed camera is triggered when the servo control system works, and all the loading or unloading processes are recorded for the maximum shear stress (τ_{max}) analysis. The acquisition resolution of the high-speed camera is 512 × 512 pixels, and the frame rate is 300 frames per second.

A total of 42 loading conditions are listed in Table 2. The final stress state after the loading tests serves as the initial stress state for the unloading tests. Therefore, this study includes 42 sets of loading to shear unloading cycles and 42 sets of loading to vertical unloading cycles, totaling 84 tests. The potential risk of induced seismicity will be analyzed with the following methods. Firstly, fault failure conditions are commonly expressed based on the Mohr–Coulomb failure criterion.[25,36,37] The relationship between normal and shear stress on the simulated fault is measured by sensors and can be used to discuss the potential occurrence of failure. Secondly, since photoelastic experiments can only be conducted within the elastic stage, this study identifies the potential risk of fault failure by confirming stress concentration regions, where rupture failure is prone to occur.[64–66] Even with very small displacements, rapid stress variations in stress concentrations can exceed the shear strength and lead to failure. The unreplaceable advantage of

Table 2
Geometric parameters of the fault surface and loading condition.

Specimen	Nominal JRC	Teeth number	Undulating angle (°)	Shear displacement (mm)	Initial normal stress (MPa)
A 1-1	9.6	2	11.3	2	0.8
A 1-2					1
A 1-3					1.2
A 2-1				4	0.8
A 2-2					1
A 2-3					1.2
B 1-1	11.2	2	14.0	2	0.8
B 1-2					1
B 1-3					1.2
B 2-1				4	0.8
B 2-2					1
B 2-3					1.2
C 1-1	13.2	2	18.4	2	0.8
C 1-2					1
C 1-3					1.2
C 2-1				4	0.8
C 2-2					1
C 2-3					1.2
D 1-1	16.2	2	26.6	2	0.8
D 1-2					1
D 1-3					1.2
D 2-1				4	0.8
D 2-2					1
D 2-3					1.2
E 1-1	16.2	3	18.4	2	0.8
E 1-2					1
E 1-3					1.2
E 2-1				4	0.8
E 2-2					1
E 2-3					1.2
F 1-1	19.1	3	26.6	2	0.8
F 1-2					1
F 1-3					1.2
F 2-1				4	0.8
F 2-2					1
F 2-3					1.2
G 1-1	0	0	0	2	0.8
G 1-2					1
G 1-3					1.2
G 2-1				4	0.8
G 2-2					1
G 2-3					1.2

photoelastic lies in its ability to directly observe and determine the location of stress concentration regions through observation of fringe order variation. Additionally, this study determines the occurrence of unloading induced seismicity through the sudden release of energy. Research indicates that the energy released during an earthquake is proportional to the shear stress drop.[67–69] When a sudden relative slip occurs on the simulated fault, a significantly shear stress drop occurs within the specimen compared to subsequent slips, which can be verified by observing the variation in fringe order in the photoelastic images.

All of the tests are repeated three times under the same condition. The data is considered valid when the difference between the mean and median is less than 5 %. R Reproducibility in the elastic stage is an important advantage of photoelastic experiments. The polycarbonate material used in this experiment is characterized by homogeneity and isotropy and the fracture surfaces are designed and machined using a lathe with a precision of 0.001 mm. The repeatability tests include the processes of loading to unloading in shear direction and loading to unloading in vertical direction. In the repeat tests, the measured

parameters included the shear force and normal force obtained from the pressure sensors, and the fringe orders at reference points. The median and mean values of these data will be compared to confirm their validity. In fact, for the same specimen under identical normal and shear displacements, these parameters are nearly the same. Testing results can also prove this.

3. Experimental result

To simulate the seismicity induced by loading and unloading conditions and to investigate the influence of fault morphology in this process, 84 tests with different $\sigma_{Ninitial}$ and S_d are conducted. During these tests, the forces in normal and shear directions are directly measured by force sensors, and the high-speed camera completely records the isochromatic fringe patterns that appeared in the process.

Three possibilities for inducing earthquakes will be discussed in this chapter. The first possibility is that shear failure occurs on the fault surface due to the movement of the pre-existing fault, which can be explained by the movement of Mohr circles (Fig. 4a). Fault instability occurs when the shear stress on the fault exceeds the frictional strength. The changes in normal stress and shear stress on the fault surface are affected by factors such as morphology, boundary conditions, and form of stress change. The second possibility is that shear failure occurs in the stress concentration region when the maximum shear stress (τ_{max}) exceeds the shear strength. Research has shown that stress concentration regions play a crucial role in locating induced seismicity.[66,70,71] During the loading process, the increase in τ_{max} in the stress concentration region was significantly larger than other regions, which behaved as rapid increase of fringe order. Since the fundamental premise of photoelastic experiments is the elastic stage, this test can only identify potential simulated fault failure regions rather than confirm actual fractures. The third possibility involves a simulated fault in a critical stress state undergoing stress changes, which can result in sudden slip

along the fault surface. This sudden slip is characterized by a rapid release of energy and can be directly observed through visualization of stress drop of τ_{max}[67–69]。 In these tests it manifests as a rapid reduction in the fringe order in the stress concentration area at the moment of instability compared to the subsequent sliding.

It is worth mentioning that despite the contact area changing during sliding, the toothed model can be simplified (Fig. 4b). The resolved normal force F_N^1 and shear force F_S^1 are calculated based on the undulation angle of the teeth and the forces measured by sensors. The measured forces are not decomposed for convenience of engineering application in this chapter but will be discussed in Chapter 4.

3.1. Control group (group G)

Group G (Fig. 5) is set as the control group of this research to distinguish the characteristics of fault slip and elastic deformation during the experiment. Group G can be seen as a special case in which the undulation angle α equals 0. Thus, the reference group is the most simplified and has the fewest variables. The contact surface of this group is straight and without teeth. The elastic deformation and slip in the stress change process can be determined by optical, geometric and mechanical characteristics.

3.1.1. Optical feature
Although the simulated fault for Group G is straight and smooth, scratches produced by cutting make small invisible bumps. After applying the initial normal force, the blocks are compressed, and the bumps on the contact surface squeeze against each other. The normal elastic deformation of blocks increases with the increasing normal force, and a concentration of shear stress is generated around the contact surface because of the interaction of bumps in the shear direction. From Fig. 5, the fringe propagates perpendicular to the contact surface in this
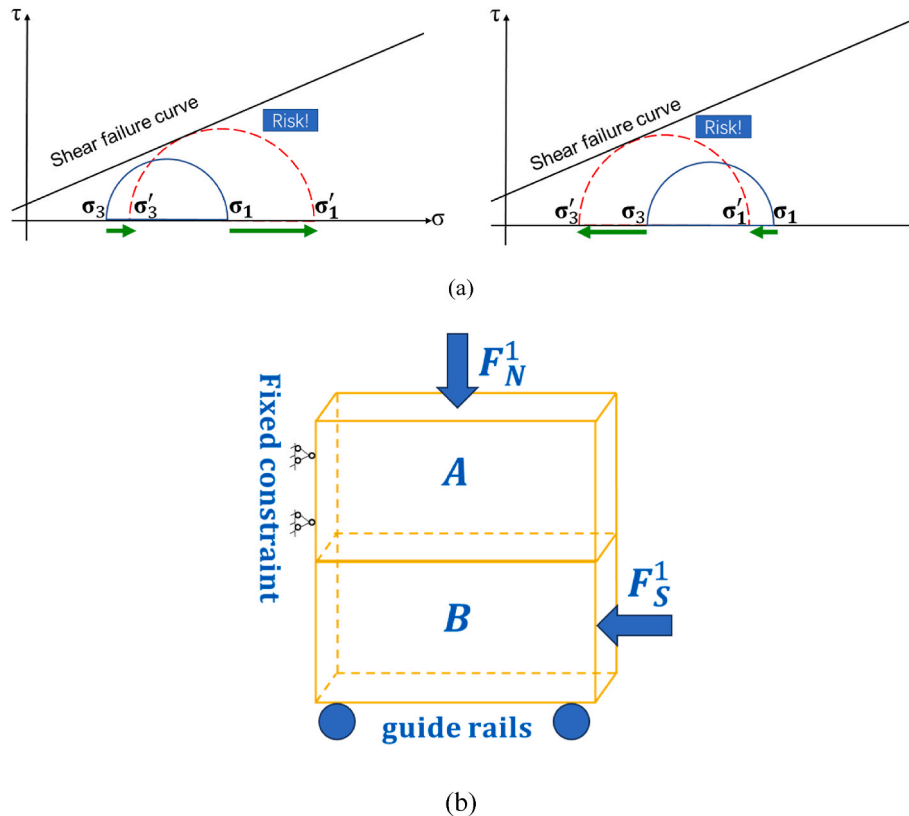

(a)

(b)

Fig. 4. Schematic of (a)Mohr–Coulomb failure criterion. The solid circle moves towards the failure curve when stress changes (b)the loading conditions in the shear test.
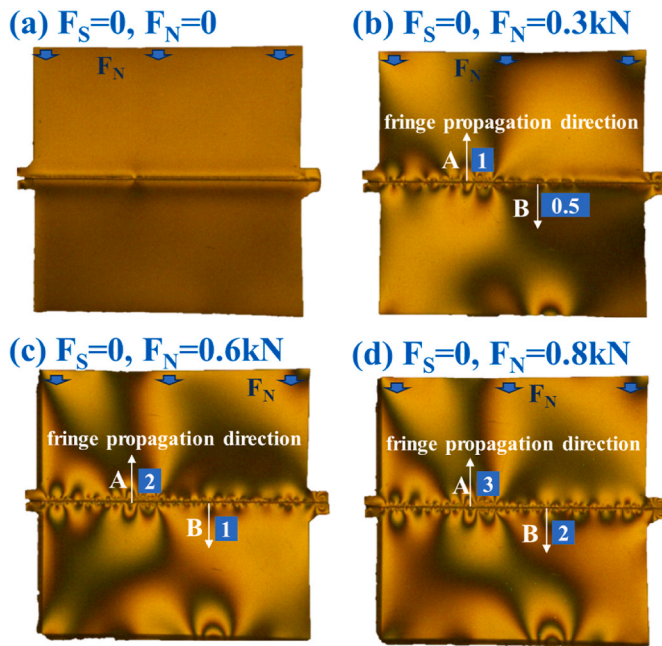
Fig. 5. Fringe variation of sample G2-1 during normal loading (a)F_N = 0 kN, (b)F_N = 0.3 kN, (c)F_N = 0.6 kN, (d)F_N = 0.8 kN. The numbers represent the fringe order.

process. The fringe order for reference points adjacent to the contact surface increases with increasing normal force, which means the increase of the maximum shear stress inside the block.

Then, the driving block controlled by the servo control system advances for 4 mm at 1 mm/s. Before sliding, F_N fluctuates slightly around $F_{N\ initial}$, and the F_S increases. Then the driving block starts sliding, the normal force decreases slightly and eventually remains unchanged. As recorded by the high-speed camera (Fig. 6), the fringe sway slightly from side to side in the shear process and the fringe order for reference point does not change. This phenomenon indicates that the maximum shear stress along the simulated fault is nearly constant during sliding.

3.1.2. Mechanical feature

The forces in normal and shear directions can be directly measured by force sensors located in two directions. Test results of the reference
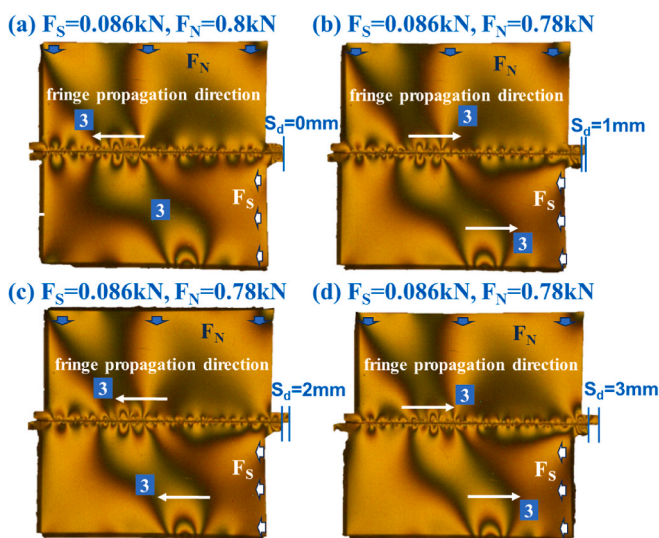
Fig. 6. Fringe variation of sample G2-1 in the shear process (a)S_d = 0 mm, (b) S_d = 1 mm, (c) S_d = 2 mm, (d) S_d = 3 mm. The numbers represent fringe order.

group are shown in Fig. 7. The force-displacement curve includes two stages: when $F_{N\ initial}$ = 0.8 kN, OA in Fig. 7a refers to the shear force accumulation phase, in which the shear force increases monotonically up to the maximum shear force. AB in Fig. 7a is the slip phase, where the shear displacement increases while the shear force is almost unchanged. In the slip phase, with various $F_{N\ initial}$, the coefficient of sliding friction $\mu = \frac{F_S}{F_N}$ is almost the same. From Fig. 7b, when $F_{N\ initial}$ = 0.8 MPa, F_S = 0.086 MPa, F_N = 0.778 MPa, and μ = 0.086/0.778 = 0.110. Similar, when $F_{N\ initial}$ = 1 MPa, μ = 0.111/0.979 = 0.113, and when $F_{N\ initial}$ = 1.2 MPa, μ = 0.136/1.184 = 0.114.

For shear unloading cases, when the constraint in the shear direction retreats, the sliding stops immediately. F_N is slightly reduced, F_S = 0 and the fringe stops shaking at once. There is no rebound in the shear direction. For vertical unloading cases, the constraint in the vertical direction retreats, the fringes disappear gradually, and the shear displacement first increases slightly and then remains unchanged (Fig. 8).

3.2. Characteristics for loading phase

Test result of D1-1, which is recorded by a high-speed camera, is used to illustrate the loading process. The two blocks are pressed and fully interlocked by applying a servo-controlled $F_{N\ initial}$ on the upper block. A certain amount of elastic energy is stored, and no slip appears. As shown from Fig. 9a–9d, the fringes develop along the loading direction and are approximately symmetrical during this process, which is consistent with the reference group. Then, the driving block is advanced for 2 mm with a shearing rate of 1 mm/s. The shear process is shown from Fig. 9e–9h. The normal force and shear force are both increasing because the normal displacement is constrained. The increasing direction of the fringe order changes from vertical to perpendicular to the contact surface, and the fringe sways parallel to the contact surface simultaneously. The comparison of contour for sample D1-1 before and after shearing is shown in Fig. 10a, in which the slip distance (S_{d1}) is much larger than the elastic deformation (V_{d1}), and the length of the contact surface decreases with increasing shear displacement. As shown in Fig. 10b, the measured forces are decomposed in directions along and perpendicular to the contact surface. This displacement-force curve includes three stages: shear force accumulation, slip and deformation slip. The shear force accumulation stage is the phase in which shear force gradually reaches the first peak, the shear deformation increases and the friction type changes from motionless to sliding. The slip stage refers to the stage in which the shear force changes slightly while the shear displacement continuously increases. The length of the slip stage is decided by the undulation angle. The deformation slip stage is the stage in which the normal deformation increases with increasing shear displacement. The normal force increases with increasing normal deformation, and the required shear force also increases as sliding friction still occurs at the contact surface. The deformation slip stage ends when the shear stress exceeds the shear failure strength of the fault. According to the optical, mechanical and geometric features, elastic deformation and relative displacement of simulate fault simultaneously occur in the loading process.

The shear displacement in this study are 2 mm and 4 mm. Since the mechanical curves for the 4 mm are very similar to the 2 mm, and the 2–4 mm section is merely a linear extension, only the measurement results for the 2 mm shear distance are presented here to save space. When the shear displacement is 2 mm, as shown in Fig. 11, the forces are redistributed during the initial stage of the loading process, corresponding to the shear force accumulation and slip stage. The shear force increases with increasing shearing displacement, while the normal force fluctuates at the beginning and then increases with increasing shear displacement. This is caused by the change in friction type and the increase in shear deformation. Additionally, as seen in Fig. 12, at the onset of loading, the fringe along the fault, whose order represents maximum
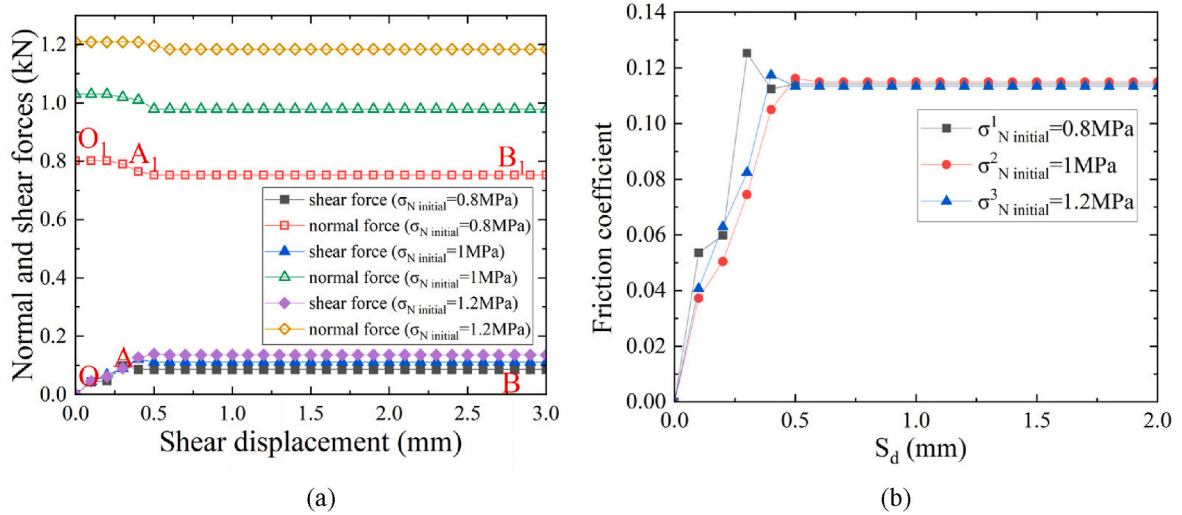
(a)

(b)

Fig. 7. (a)Measured forces in normal and shear directions, and (b) friction coefficient for samples G2-1, G2-2, and G2-3 in the loading process.
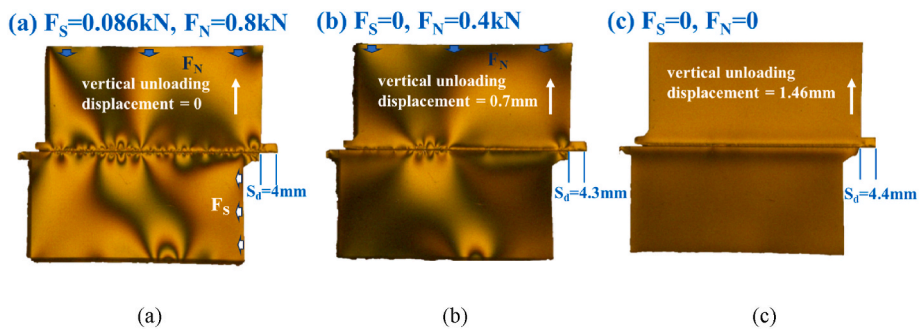

(a)

(b)

(c)

Fig. 8. Fringe variation of sample G2-1 in the vertical unloading process, in which vertical unloading displacement = (a) 0 mm, (b)0.7 mm, (c)1.46 mm.
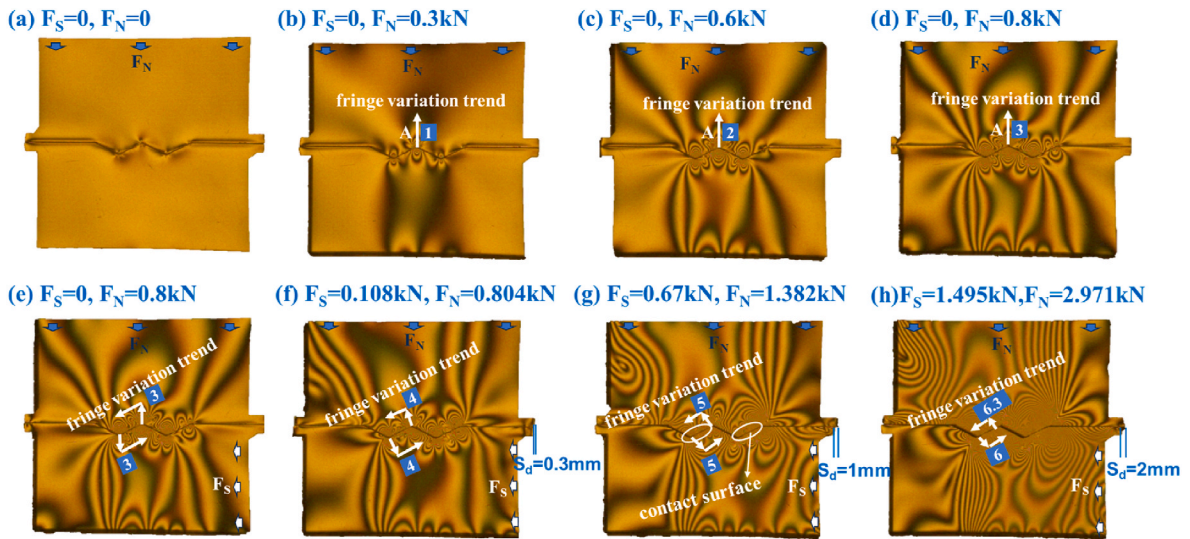

Fig. 9. Fringe variation of sample D1-1, (a) to (d) application of $F_{N\ initial}$, (e) to (h) shear process.

shear stress, does not have order change but oscillates from side to side. The driving block slips along the contact surface when the shear force and normal force along the fault reach a specific ratio. The shear and normal forces then increase proportionally as shear displacement increases, corresponding to the deformation slip stage. The contact surface length continues to decrease, and the stress concentration phenomenon

occurs perpendicular to the contact surface.

Though the undulation angle, teeth number, and contact area of each experiment group are different during sliding, the measured forces (Fig. 13) indicate that all the sliding friction models can be simplified to the model mentioned above (Fig. 4b). When the driving block is continued to slide, F_S^1 and F_N^1 increase proportionally, corresponding to
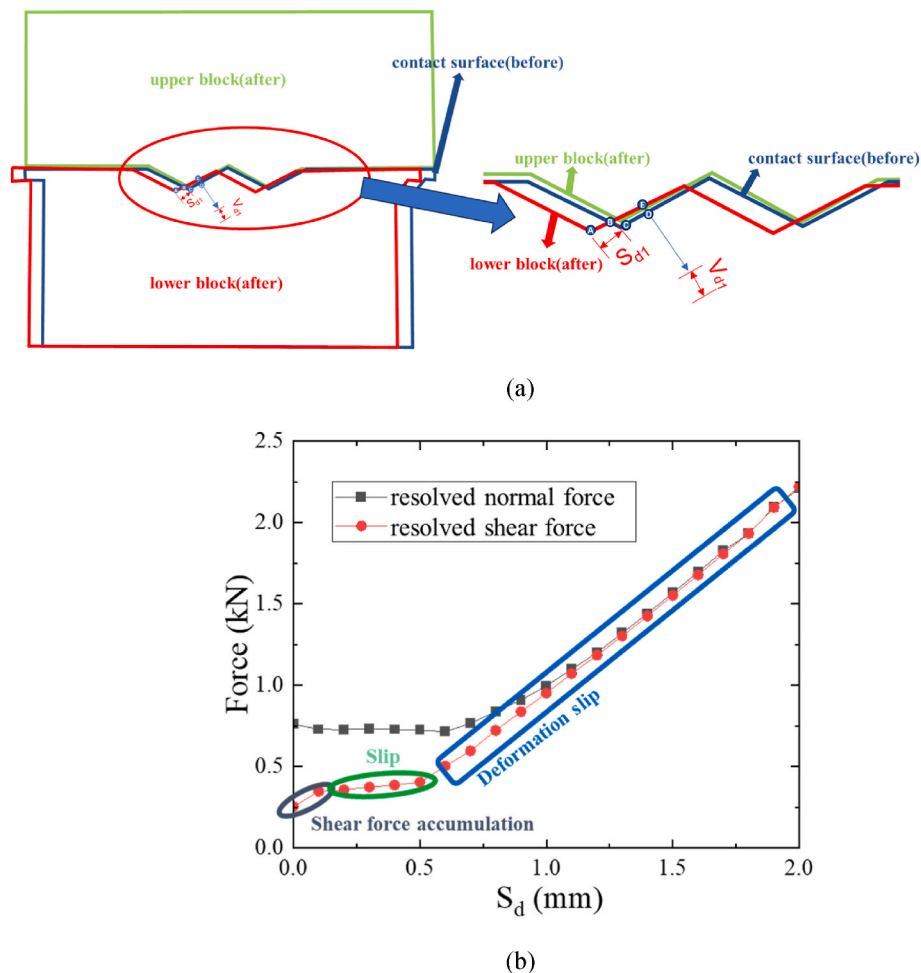
(a)

(b)

Fig. 10. (a)Comparison of contour of sample D1-1 before and after shear. The blue line is the contour of the contact surface before shearing. The green line is the contour of the upper block, and the red line is the contour of the lower (driving) block. The S_{d1} is the relative shear displacement parallel to the contact surface, and the V_{d1} is the relative deformation perpendicular to the contact surface. (b) The resolved force of sample D1-1 in the loading process. (For interpretation of the references to colour in this figure legend, the reader is referred to the Web version of this article.)

the deformation slip stage mentioned above. The sliding friction coefficient of the simplified model for different groups is calculated by $\mu_0 = \frac{F_S}{F_N}$ and listed in Table 3. The theoretical coefficient of sliding friction is calculated by

$$\mu = tan\,(\alpha + \varphi_0) \qquad (7)$$

where φ_0 denotes the friction angle of a flat and straight joint (Group G). According to Table 3 and Fig. 13, μ_0 is not influenced by $\sigma_{N\ initial}$ and S_d but affected by undulation angle. Due to the cumulative elastic deformation, the teeth number has a small effect on the friction coefficient. The μ_0 increased with increasing JRC, and the effect of the undulation angle is greater than the number of teeth. The μ_0 is higher for samples with the same JRC when the teeth number is small.

The fault slip burst is defined as a rock burst caused by the movement of the pre-existing fault or the formation of earthquake-prone structural zones.[40] Fault slip burst is prone to occur at stress concentration regions. To analyze stress concentration region and maximum shear stress, the change of fringe order is captured with the high-speed camera. In Fig. 14a, six reference points (OA=OB=O_1A_1 = O_1B_1=O_2A_2 = O_2B_2= 10 mm) are selected from group A for stress concentration analysis.

According to Saint Venant's Principle, for reference points in stress concentration region (A, B_1, and A_2), the fringe order, which is proportional to maximum shear stress, increased with increasing shear displacement (S_d) and $F_{N\ initial}$. For reference points located in other

regions (B, A_1, and B_2), the fringe order is slightly influenced by S_d and $F_{N\ initial}$ (Fig. 14c). Besides, the maximum shear stress in the middle region is generally larger than that at other places. Experiment results indicate that the stress concentration regions are the mini slopes distributed perpendicular to the contact surface rather than the entire fault (Fig. 14b). The value of maximum shear stress and area of stress concentration region is controlled by the teeth number and undulation angle. Data from other groups show the same regularity.

Research indicate that each fracture can be considered as a seismogenic element.[72] The Coulomb failure criterion is used to determine whether a defect or small fault will transform into a seismic event.[73] Based on the experimental results, potential risk of induced seismicity exists during the loading process. The first potential possibility of induced seismicity is the occurrence of shear failure in the stress concentration regions. For deep underground engineering or rock masses supported by anchor bolts, the dilatant deformation during fault shear slip is constrained by the surrounding rock and the anchoring structure. Even with small shear displacement, the τ_{max} in the stress concentration regions can significantly increases, which may exceed the shear strength of the rock mass and causing fractures. The second possibility can be explained by the Mohr-Coulomb failure criterion (Fig. 15). When the fault is subjected to external loads in the shear direction, the upper rock mass or soil is compressed, producing shear elastic deformation, and the contact surface becomes fully interlocked. With increasing shear displacement, the Mohr circle moves towards the failure envelope,
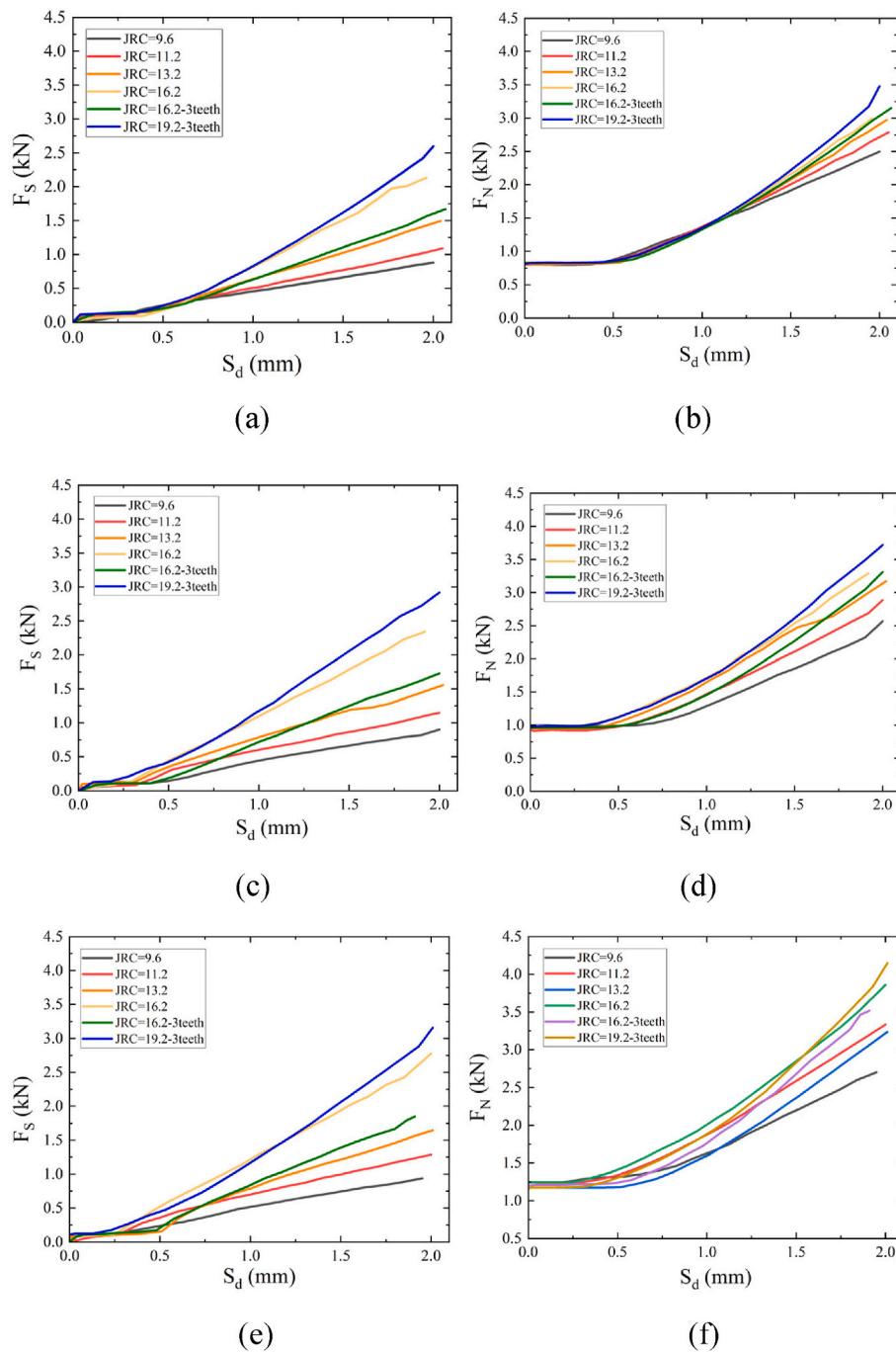
Fig. 11. Measured forces in normal and shear directions for all samples in the shear loading process when $S_d = 2$ mm (a) shear force, $\sigma_{N\ initial} = 0.8$ MPa, (b) normal force, $\sigma_{N\ initial} = 0.8$ MPa, (c) shear force, $\sigma_{N\ initial} = 1$ MPa, (d) normal force, $\sigma_{N\ initial} = 1$ MPa (e) shear force, $\sigma_{N\ initial} = 1.2$ MPa, (f) normal force, $\sigma_{N\ initial} = 1.2$ MPa.

indicating that shear failure may occur along the fault. It is important to note that K is not the reciprocal of the friction coefficient, as the length of the contact surface (Table 3) decreases with S_d. Another possibility of instability is also noted: when the fault is in a critical stress equilibrium state where the normal stress and shear stress on the fault reach a certain ratio, a sudden external disturbance can disrupt this balance, leading to sudden slip and instability. Although this experiment determined the stress ratio under critical conditions, the current equipment could not apply disturbance loads. Related disturbance experiments will be conducted after the experimental equipment[74] is upgraded.

3.3. Unloading in shear direction

Experiment results indicated that unloading in the shear direction can induce both seismicity and aseismic slip. Based on the stress state of the loading situation, i.e., $F_{N\ initial}$ is applied, and the driving block advanced for 2 or 4 mm. The position of the constraint in the vertical direction is fixed, and then the constraint in the shear direction retreats at 1 mm/s. The unloading process stops when $F_S = 0$.

The experimental results for shear unloading after a 4 mm shear displacement are similar to those after a 2 mm shear displacement. To save space, the explanation uses the experimental results for a shear displacement of 2 mm (Fig. 16). In the shear unloading process, the variation trend of F_S is three-stage for samples with lower JRC and
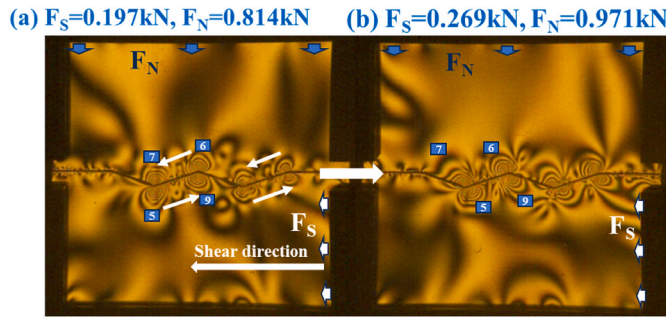
Fig. 12. The variation of the isochromatic fringe pattern of sample C1-1 (a) $\sigma_{N\ initial}$ = 0.8 MPa is applied (b) the driving block is about to slide.

undulation angle. The F_S decreases rapidly in the very beginning, and then the F_S slightly increases and decreases slowly in the last stage. With increasing JRC, the variation trend turns into two stages, i.e., F_S decreases rapidly in the first stage and decreases slowly in the second stage. The variation trend for F_N is different from shear force. F_N decreases slowly in the first stage and decreases rapidly in the second stage. The friction coefficient in the shearing stage is different from the unloading stage (Fig. 17) despite the contact area being the same most of the time. A potential explanation is that the normal and shear deformation varies during the loading and unloading due to different boundary constraints. Another possible explanation is that the direction of the relative displacement of loading and shear unloading is opposite. Many researchers believed JRC has anisotropy as the strength and failure features are completely different when shear directions vary.[75,76] Barton el al.[77] has taken shearing direction into consideration in the tilt test, and Huan et al.[78] has considered the contribution of shear direction and proposed a new parameter WPA for the estimation of JRC. Although this study is based on the elastic stage and does not involve actual fracture, the potential risk of shear unloading-induced seismicity can be illustrated using a Mohr circle (Fig. 18). When the lateral constraint removal occurs on the simulated fault where normal stress is larger than shear stress, the solid circle moves towards the failure curve at the beginning of the shear unloading process, and shear failure may happen under these circumstances.

Despite the possibility of triggering seismicity, the reduction of surface normal stress and restoration of displacement proves that unloading in the shear direction also has aseismic features. The high-speed camera records the shear unloading process (Fig. 19), and the maximum shear

stress is slightly decreased compared to the stage when the $\sigma_{N\ initial}$ is applied. The shear displacement caused by loading recovers stepwisely and is eventually restored to the initial state. When shear unloading ends, the contact area increases, and the residual normal stress is less than the $\sigma_{N\ initial}$. When the $\sigma_{N\ initial}$ increases, the amount of compression and the elastic energy stored in the loading process increases. Experimental results indicate that the attenuation of normal stress becomes more significant with increasing $\sigma_{N\ initial}$ (Fig. 20), suggesting that higher historic in situ stress may release more energy. This conclusion, which has essential practical engineering implications, has not been mentioned by other researchers. For instance, the risk and magnitude of induced earthquakes can be reduced by removing shear constraints adjacent to the faults in highly stressed areas.

3.4. Unloading in the vertical direction

Based on the stress state of the loading conditions, i.e., $\sigma_{N\ initial}$ is applied, and the driving block advances for 2 or 4 mm. The position of the constraint in the vertical direction retreats at 1 mm/s. The normal unloading process stops when F_N = 0 (unloading rate = 1 mm/s). In the vertical unloading process (Fig. 21), the driving block continued to advance, and the maximum shear stress decreased. The slip velocity is relatively fast at the beginning because the normal and shear deformation stored in the interdigitation region is released. The energy accumulated due to concentration is gradually released, and the fringe is nearly eliminated except for some marginal points. The measured force in normal and shear directions (Fig. 22) indicates that unloading in the normal direction will cause stress redistribution. The F_N and F_S change rapidly from the initial state to the line where the sliding friction
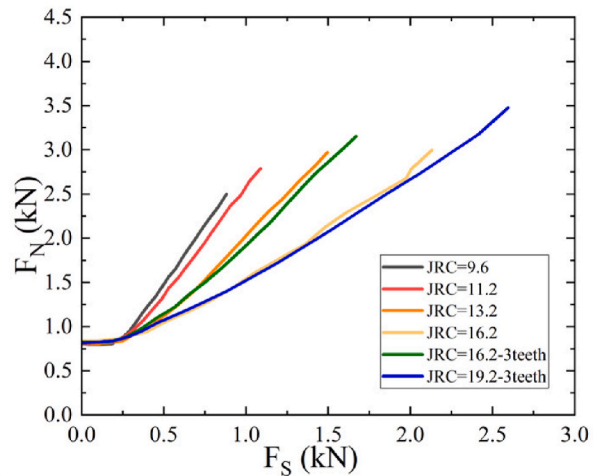
Table 3
The sliding friction coefficient of the equivalent model.

Group	Nominal JRC	undulation angle (°)	contact length (mm)	μ_0	tan ($\alpha+\varphi_0$)
A	9.6	11.3	51	0.348	0.317
B	11.2	14	41.2	0.385	0.371
C	13.2	18.4	31.6	0.493	0.461
D	16.2	26.6	22.4	0.704	0.648
E	16.2 (3teeth)	18.4	47.4	0.524	0.461
F	19.1 (3teeth)	26.6	33.5	0.735	0.648
G	0	0	100	0.11	0.11
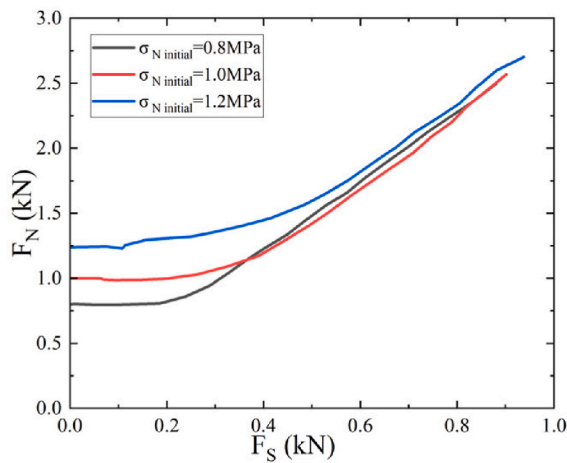
(a)

(b)

Fig. 13. Measured forces in loading process when S_d = 2 mm (a) $\sigma_{N\ initial}$ = 0.8, 1, 1.2 MPa, JRC = 9.6 (b) JRC ranges from 9.6 to 19.2, $\sigma_{N\ initial}$ = 0.8 MPa.

(a)   (b)
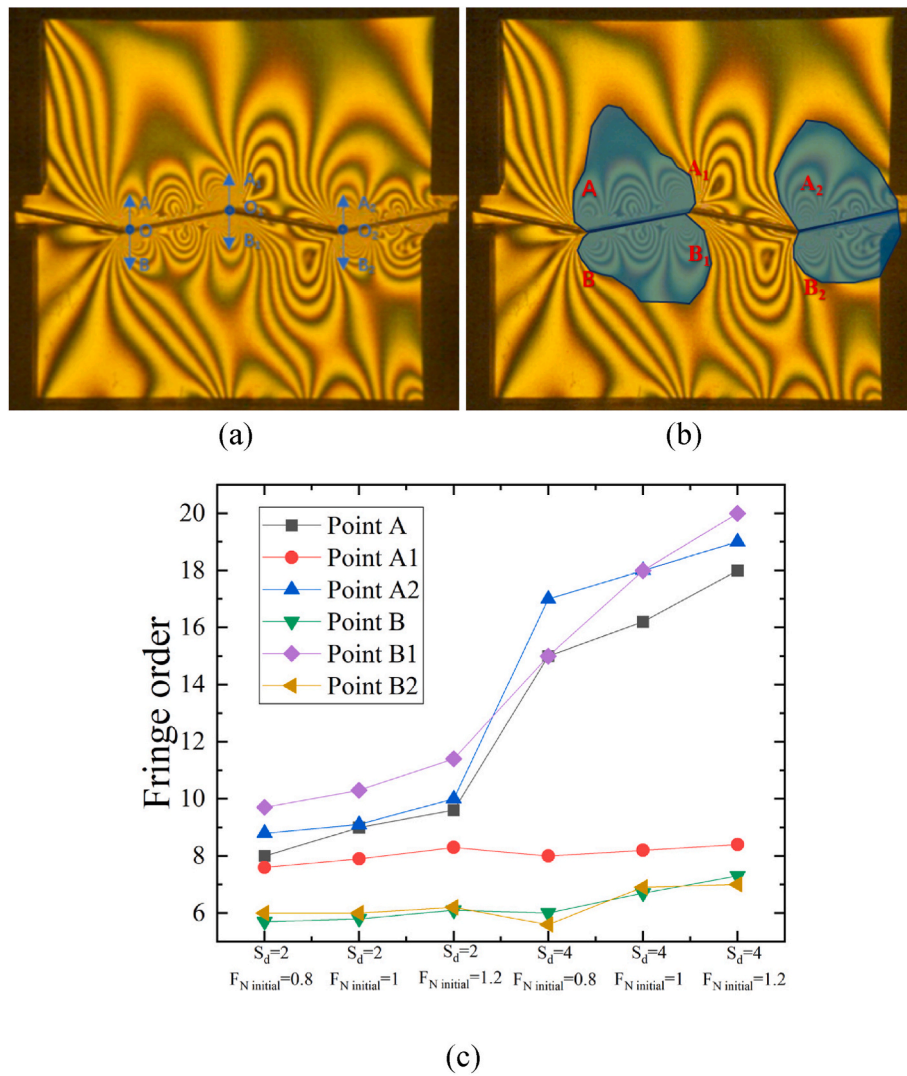

(c)

Fig. 14. (a)Reference points, (b)stress concentration regions, and (c)fringe order for reference points of group A in the loading process.
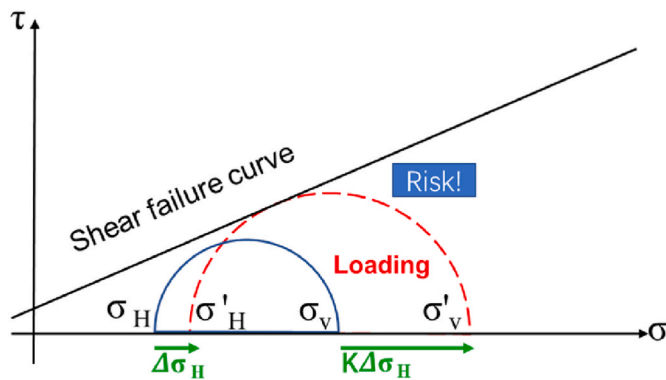

Fig. 15. Schematics of the Mohr circles showing the fault slip burst attributed to the loading process before (blue solid circle) and after (red dashed circle). (For interpretation of the references to colour in this figure legend, the reader is referred to the Web version of this article.)

coefficient $\mu_2 = \frac{F_{S2}}{F_{N2}}$ is constant. The μ_2 is not influenced by $\sigma_{N\ initial}$ or S_d but is mainly controlled by the undulation angle. Nonetheless, μ_2 in the vertical unloading process is slightly lower than μ_1 in the loading process and is larger than the shear unloading process (Fig. 23). According to the

results recorded by the high-speed camera, the direction of the relative displacement between the upper and lower test blocks during the vertical unloading process is consistent with that during the loading process, but opposite to the direction of relative displacement during the shear unloading process. This also verifies that JRC has anisotropy feature when shear directions vary.

Although the samples with different teeth numbers have a close sliding friction coefficient when the undulation angle is the same, the reduction rate of vertical stress has a significant difference. The stress reduction rate refers to the rate at which the normal stress on the simulated fault surface decreases when the normal constraint on the sample is removed at a constant rate. The difference in reduction rate significantly affects the buffer distance and safety factor. The simulated fault surface is more prone to instability when the stress reduction rate is high. As shown in Fig. 24, it is more susceptible to sliding when the simulated fault surface is relatively flat. The reduction rate decreases with increasing undulation angle when the number of teeth is the same. Additionally, the number of teeth significantly affects the stress reduction rate. Although the samples with different numbers of teeth have a close sliding friction coefficient when the undulation angle is the same, the reduction rate of normal stress has a significant difference. The two-tooth specimen with a JRC of 13.2 and the three-tooth specimen with a JRC of 16.2 have the same undulation angle, as well as the two-tooth specimen with a JRC of 16.2 and the three-tooth specimen with a JRC
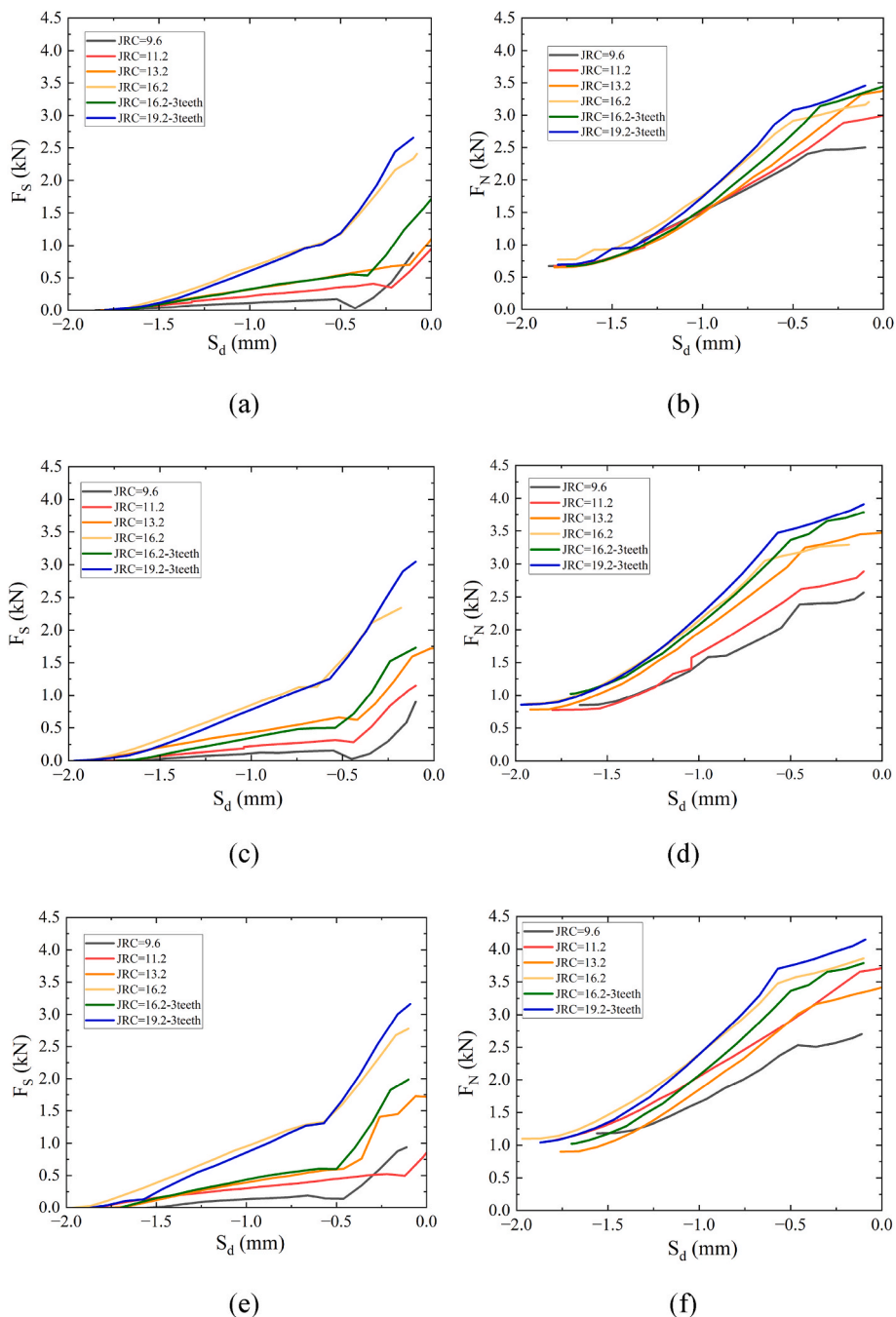
Fig. 16. Measured forces in normal and shear directions for all samples in the shear unloading process when $S_d = 2$ mm (a) shear force, $\sigma_{N\ initial} = 0.8$ MPa, (b) normal force, $\sigma_{N\ initial} = 0.8$ MPa, (c) shear force, $\sigma_{N\ initial} = 1$ MPa, (d) normal force, $\sigma_{N\ initial} = 1$ MPa (e) shear force, $\sigma_{N\ initial} = 1.2$ MPa, (f) normal force, $\sigma_{N\ initial} = 1.2$ MPa.

of 19.1, the reduction rate of surface normal stress increases as the number of teeth increases.

Vertical unloading-induced seismicity includes two possibilities. Unlike typical simulations of unloading-induced seismicity,[37] this simulation started with a critical stress state. The decrease of normal stress disturbed the frictional equilibrium of the fault, leading to sudden slip. Based on the changes in fringe order, a significant amount of energy was released within the first 0.2 s of normal unloading, which corresponds to segment AB on the stress path (Fig. 23). The visualization study of energy release during induced seismicity is currently limited by the observation methods. We are still working on developing software for automatic recognition and calculation of fringe orders to enhance accuracy and reliability for subsequent studies. Another possibility of

induced seismicity can be explained by the Mohr circle (Fig. 25). In engineering activities such as quarrying operation, artificial excavation can alter the stress distribution within the strata, causing shear stress to exceed normal stress in localized areas. This can induce shallow fault slip when vertical stress is reduced. On April 7, 1981, a diatomite quarry near Lompoc, California, experienced an M_L 2.5 earthquake, which was evidently triggered by crustal unloading.[79] The decrease in normal stress caused by this removal of diatomite is larger than the stress drops in shear stress, which show certain similarities to the case in this simulation. it should be noted that, due to the lack of firsthand data, this can only be considered a possible explanation.
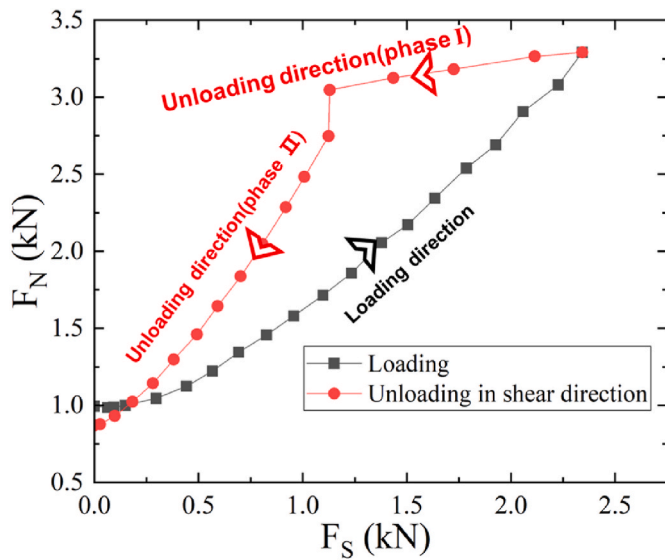
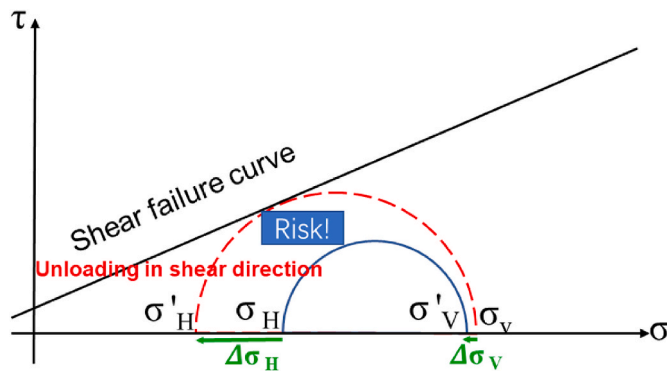**Fig. 17.** Force path of loading and unloading in shear direction for sample D1-2.

Fig. 18. Schematics of Mohr-Coulomb circles showing the fault slip burst attributed to the shear unloading process (phase I in Fig. 17) before (blue solid circle) and after (red dashed circle). (For interpretation of the references to colour in this figure legend, the reader is referred to the Web version of this article.)

4. Disscussion

Although predicting the occurrence of induced seismicity and measuring the energy of induced seismic events have long been difficult, given the complexity of underground space, the results of this study provide the possibility of identifying hazardous regions and controlling

the maximum magnitude of stress change-induced seismicity. For injection-induced seismicity, researchers have made progress in predicting and controlling the magnitude of induced seismicity. McGarr and Barbour[34] concluded that the cumulative seismic moment response to fluid injection is limited according to $\sum M_0(max) = 2G\Delta V$ when injecting volumes ranging from 1 ml to 12 million m^3, where G is the shear modulus and ΔV is the volume of fluid injected. Kwiatek et al.[80] controlled a series of induced earthquakes in a 6.1-km-deep geothermal project near Helsinki, Finland. The injection rate and amount were controlled by monitoring the earthquake rate, magnitude, hydraulic energy, and seismic evolution. Zhu et al.[69] conducted laboratory experiments and found that increasing water injection cycles can control the magnitude and energy of injection-induced earthquakes.

Since the simulated fault in photoelastic experiments is planar and no fractures form during photoelastic testing, resulting in no fracture energy, this study is suitable for simple model.[67,68] The total radiated seismic energy and the moment magnitude released at stress change induced seismicity can be calculated using maximum shear stress drop, fault area, and incremental fault slip with the following equations:

$$E_S = r_a \Delta d A \tag{8}$$

$$r_a = 0.25\tau_{max} = 0.25 * \Delta N * f_d \tag{9}$$

$$log_{10}E_s = 1.5M_w + 4.8 \tag{10}$$

Where E_s is the total radiated seismic energy, r_a is the apparent stress and equal to a quarter of the maximum shear stress drop, Δd is the incremental fault slip, A is the fault area, ΔN is the extinction order, f_d is
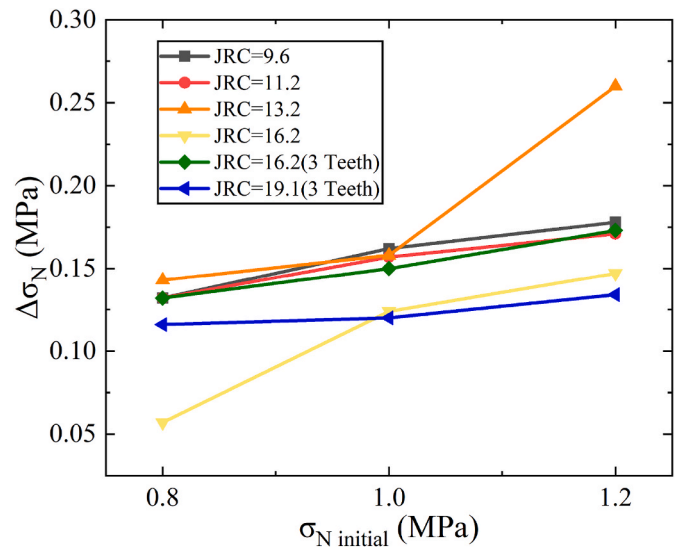

Fig. 20. Attenuation of surface normal stress ($\Delta\sigma N$) when $S_d = 2$ mm.

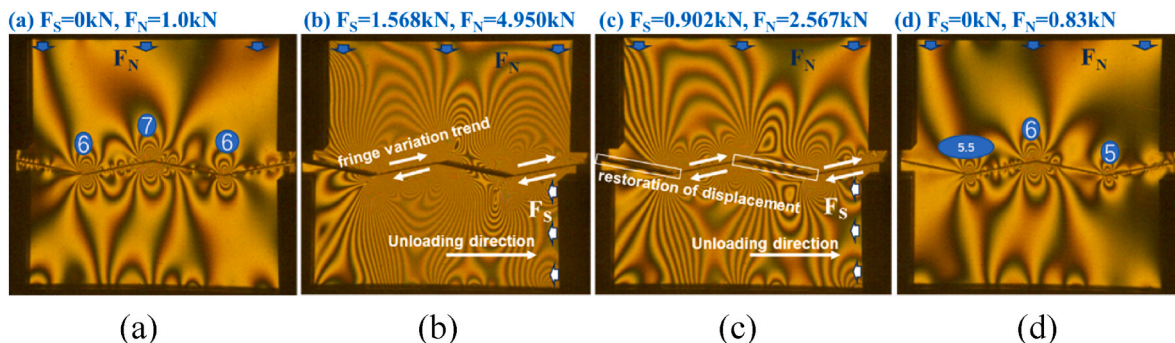**Fig. 19.** The isochromatic fringe pattern for sample A2-2 (a) under $\sigma_{N\ initial}$, and shear unloading for (b)0 mm, (c)2 mm, (d)4 mm.
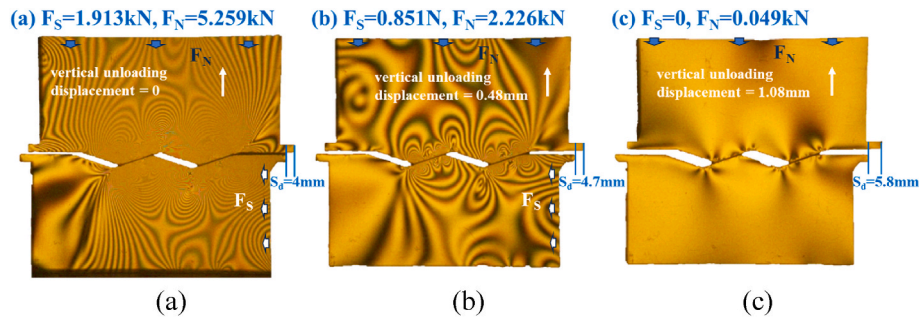
Fig. 21. The variation of isochromatic fringe pattern for vertical unloading of sample C2-2 after retreating for (a)0 mm, (b)0.8 mm, and (c)1.5 mm.
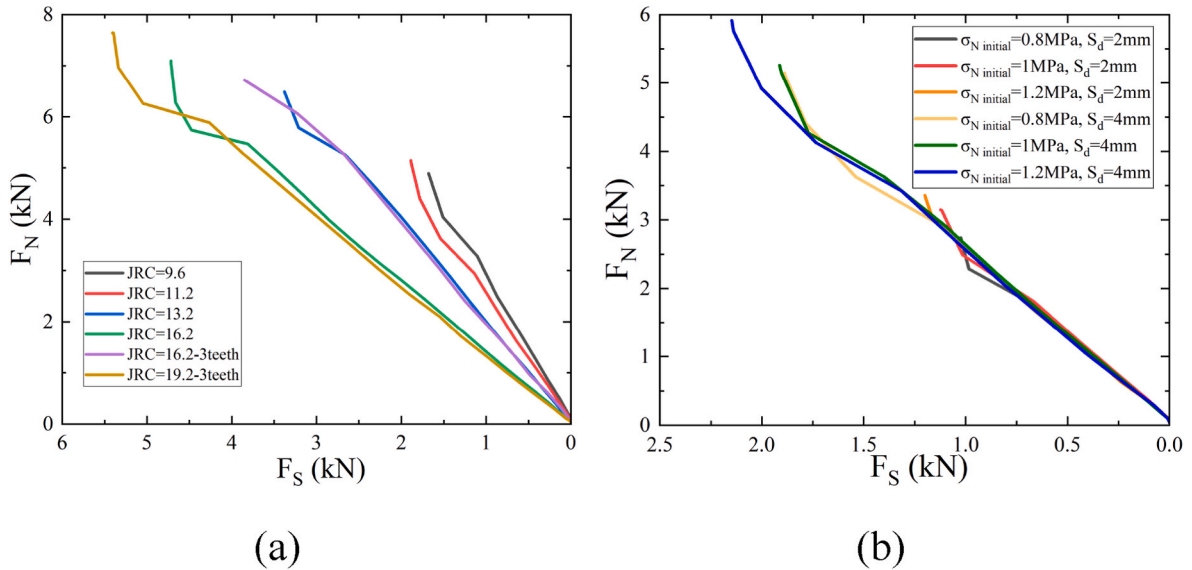

Fig. 22. Measured forces in normal and shear directions during vertical unloading (a) $\sigma_{N\ initial}$ = 0.8 MPa and S_d = 2 mm, (b) JRC = 11.2.
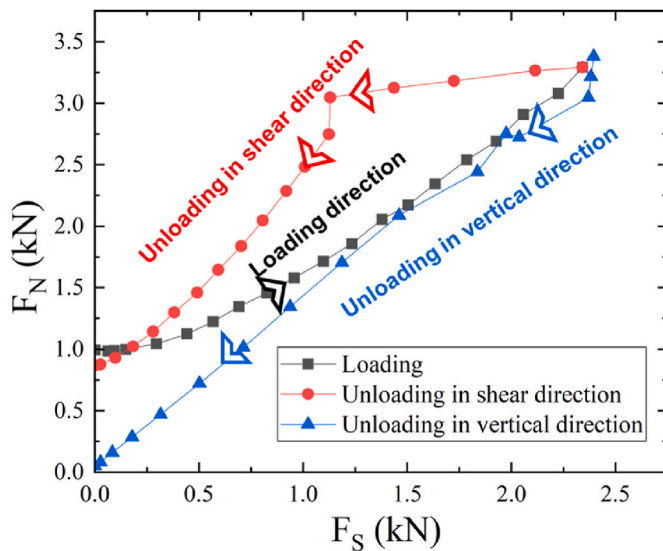

Fig. 23. Force path of loading, unloading in shear direction and unloading in vertical direction for sample D1-2.

the material fringe value in N/mm/fringe, and M_w is the moment magnitude.

The method of mesh division in numerical simulations is crucial for improving the accuracy of energy calculations in photoelastic tests. This can be achieved by increasing the grid density in stress concentration regions and reducing it in other areas. For example, the area of the computational unit is set as 0.2 cm × 0.2 cm in stress concentration regions, while in other regions the computational unit is set as 1 cm × 1 cm. By using Equation (8) to calculate the energy for each computational unit area and summing them up, the total energy released by the entire fault surface at the moment of the earthquake can be obtained. Subsequently, using Equation (10), the maximum magnitude of the fault surface can be estimated. In addition, induced seismicity involves instantaneous release of a large amount of energy, during which the rate of fringe order changes should be significantly higher than during stable slip processes. This characteristic can be used to determine the occurrence of induced earthquakes. The visualization study of energy release during induced seismicity is currently limited by the observation methods. We are still working on developing software for automatic recognition and calculation of fringe orders to enhance accuracy and reliability for subsequent studies.

Our experiments directly observed the evolution of maximum shear stress and identified the stress concentration region, which has the potential to localization of the hazardous regions. Additionally, the simplified model proposed in this research can be used to predict the possibility of stress change-induced seismicity with Mohr-Coulomb failure criterion. The measured forces are not decomposed in most cases to facilitate the arrangement of measuring instruments and engineering applications. Nevertheless, the external forces are dissolved into directions perpendicular and parallel to the contact surface as a contrast in this part. When F_S and F_N are resolved in directions that are
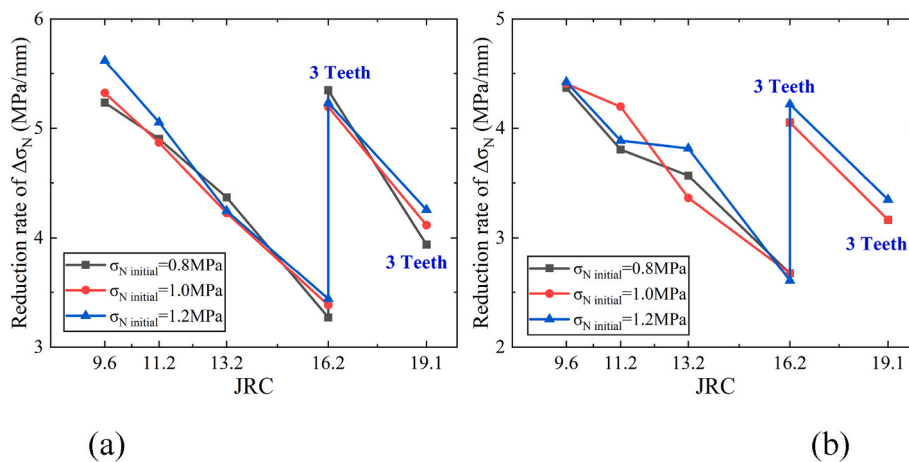
Fig. 24. The reduction rate of surface vertical stress in the vertical unloading process.
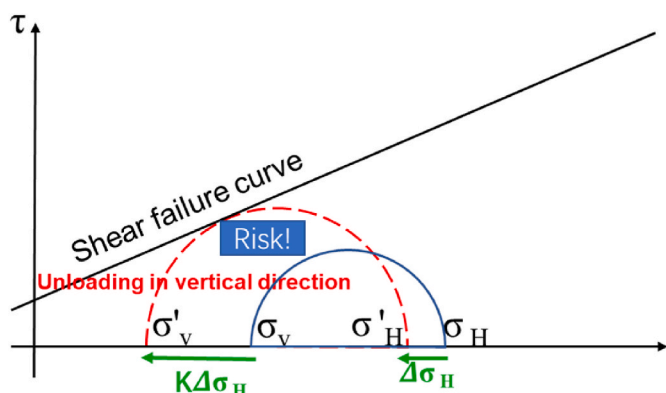

Fig. 25. Schematics of the Mohr circles showing the fault slip burst attributed to vertical unloading before (blue solid circle) and after (red dashed circle). (For interpretation of the references to colour in this figure legend, the reader is referred to the Web version of this article.)

Fig. 26. The resolved friction coefficient for all samples.

perpendicular and parallel to the contact surface, the resolved sliding friction coefficient is calculated by:

$$\mu_r = \frac{F_N \sin \alpha + F_S \cos \alpha}{F_N \cos \alpha - F_S \sin \alpha} \tag{11}$$

The sliding friction coefficient for the reference group (JRC = 0) ranges from 0.111 to 0.114. For samples with different morphology, the resolved friction coefficient mainly depends on the form of stress variation and undulation angle (Fig. 26). The friction coefficient in the vertical unloading process is close to the loading process and is larger than the shear unloading process. The friction coefficient increases with increasing undulation angle, while the teeth number has an opposite effect on the friction coefficient when the form of stress variation differs. For example, during shear unloading, the friction coefficient of the specimen with 2 teeth at 18.4° is larger than that of the specimen with 3 teeth at 18.4°. Conversely, the results are opposite during loading and normal unloading conditions.

The experimental results indicate that the reduction rate of vertical stress is very sensitive to fault morphology and initial stress state in vertical unloading cases. Thus, for human activities like quarry unloading or reservoir discharge that reduce the vertical stress, the mining or discharge velocity should be strictly controlled when the fault has slip-prone morphology or is in a high-stress field. Optimizing the unloading strategies can reduce the risk related to vertical unloading-induced seismicity. Also, based on the aseismic feature in shear loading experiments, drilling holes adjacent to the fault can release the
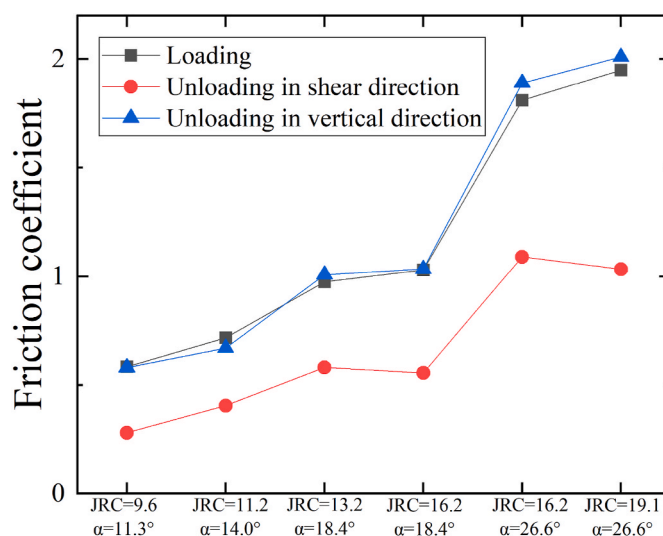
stress concentration and reduce the magnitude of induced seismicity. Installing sensors and enhancing monitoring is of great importance to guarantee the stable operation of the project, protect the existing building structure, and reduce the possibility of induced seismicity.

Although the photoelastic experiments simulate the process of fault slip and identify the risk regions, they do not reflect fracture occurrence and the cutting of rough asperities. Rock samples with the same dimension will be used in further research. Also, the induced seismicity always occurs under a complex coupling effect. The impact of environmental factors (e.g., water, temperature, moisture, fault gouge) on induced seismicity will be investigated in subsequent studies.

5. Conclusions

Using a custom direct shear machine coupled with photoelastic observation techniques, this study investigates the potential risks of induced seismicity under three different forms of stress changes: loading, shear unloading, and vertical unloading. The conclusions obtained include.

1. All forms of stress variation have the potential to induce shear failure in the simulated fault, which can be explained using the Mohr-Coulomb failure criterion. Based on sliding friction characteristics, shear failure is more likely to occur during continuous loading and

vertical unloading. In the case of shear unloading, induced seismicity caused by shear failure tends to occur at the very beginning.

2. The undulation angle has a decisive effect on the sliding friction coefficient, and the friction coefficient is affected by the form of stress variation. Due to the anisotropy of JRC and differences in boundary conditions, the friction coefficient in the vertical unloading process is close to the loading process and is larger than the shear unloading process.

3. Stress concentration regions pose a risk of induced seismicity due to shear failure. These regions can be directly identified utilizing the visualization advantages of photoelasticity and are mainly distributed perpendicular to the contact surface rather than the entire fault.

4. The reduction of surface normal stress and restoration of displacement proves that unloading in the shear direction has aseismic features. The attenuation of normal stress becomes more significant with increasing initial normal stress, suggesting that higher historic in situ stress may release more energy. This conclusion, which has essential practical engineering implications, has not been mentioned by other researchers. shear unloading also exhibits aseismic features.

5. The possibility of fault slip inducing seismicity during vertical unloading can be determined through the sudden release of energy, identifiable through a rapid change in fringe order. Visualizing and calculating the energy release during induced seismicity is feasible, though current accuracy is limited by observation methods. The accuracy and reliability will be enhanced after developing software for automatic recognition and calculation of fringe orders.

6. In vertical unloading cases, the reduction rate of surface vertical stress decreases with increasing undulation angle when the teeth number is the same and increases with the number of teeth when the undulation angle is the same. The difference in reduction rate greatly influences the buffer distance and safety factor in human activities.

CRediT authorship contribution statement

Dapeng Wang: Writing – original draft, Validation, Methodology, Investigation, Formal analysis, Data curation, Conceptualization. **Jianchun Li:** Writing – review & editing, Visualization, Supervision, Resources, Project administration, Investigation, Funding acquisition, Formal analysis, Conceptualization. **Chunjiang Zou:** Writing – review & editing, Writing – original draft, Supervision, Software, Project administration, Methodology, Investigation, Formal analysis, Data curation, Conceptualization. **Zhijie Wang:** Visualization, Validation, Software, Investigation, Data curation. **Jian Zhao:** Writing – review & editing, Supervision, Resources, Project administration, Methodology, Formal analysis, Conceptualization.

Declaration of competing interest

The authors declare that they have no known competing financial interests or personal relationships that could have appeared to influence the work reported in this paper.

Data availability

Data will be made available on request.

Acknowledgements

References

1. Keranen KM, Savage HM, Abers GA, et al. Potentially induced earthquakes in Oklahoma, USA: links between wastewater injection and the 2011 Mw 5.7 earthquake sequence. *Geology*. 2013;41(6):699–702.
2. Keranen KM, Weingarten M, Abers GA, et al. Sharp increase in central Oklahoma seismicity since 2008 induced by massive wastewater injection. *Science*. 2014;345 (6195):448–451.
3. Skoumal RJ, Brudzinski MR, Currie BS. Microseismicity induced by deep wastewater injection in southern trumbull county, Ohio. *Seismol Res Lett*. 2015;86(5): 1326–1334.
4. Segall P. Earthquakes triggered by fluid extraction. *Geology*. 1989;17(10):942–946.
5. Segall P, Fitzgerald SD. A note on induced stress changes in hydrocarbon and geothermal reservoirs. *Tectonophysics*. 1998;289(1-3):117–128.
6. Jiao Y-Y, Wu K, Zou J, et al. On the strong earthquakes induced by deep coal mining under thick strata-a case study. *Geomechanics and Geophysics for Geo-Energy and Geo-Resources*. 2021;7(4):97.
7. Zou J, Wu K, Zhang X, et al. Effective evaluation of deep-hole blasting for controlling strong tremors induced by deep coal mining-A case study. *Int J Rock Mech Min Sci*. 2022;159, 105211.
8. Ge S, Liu M, Lu N, et al. Did the zipingpu reservoir trigger the 2008 wenchuan earthquake? *Geophys Res Lett*. 2009;36(20). np-n/a.
9. Gupta HK. A review of recent studies of triggered earthquakes by artificial water reservoirs with special emphasis on earthquakes in Koyna, India. *Earth Sci Rev*. 2002; 58(3):279–310.
10. Diehl T, Kraft T, Kissling E, et al. The induced earthquake sequence related to the St. Gallen deep geothermal project (Switzerland): fault reactivation and fluid interactions imaged by microseismicity. *J Geophys Res Solid Earth*. 2017;122(9): 7272–7290.
11. Rathnaweera TD, Wu W, Ji Y, et al. Understanding injection-induced seismicity in enhanced geothermal systems: from the coupled thermo-hydro-mechanical-chemical process to anthropogenic earthquake prediction. *Earth Sci Rev*. 2020;205, 103182.
12. Li X, Li C, Parriaux A, et al. Multiple resources and their sustainable development in Urban Underground Space. *Tunn Undergr Space Technol*. 2016;55:59–66.
13. Lu S-M. A global review of enhanced geothermal system (EGS). *Renew Sustain Energy Rev*. 2018;81:2902–2921.
14. Menéndez J, Ordóñez A, Álvarez R, et al. Energy from closed mines: underground energy storage and geothermal applications. *Renew Sustain Energy Rev*. 2019;108: 498–512.
15. Zhang C, Wang F, Bai Q. Underground space utilization of coalmines in China: a review of underground water reservoir construction. *Tunn Undergr Space Technol*. 2021;107, 103657.
16. Deichmann N, Giardini D. Earthquakes induced by the stimulation of an enhanced geothermal system below Basel (Switzerland). *Seismol Res Lett*. 2009;80(5):784–798.
17. Häring MO, Schanz U, Ladner F, et al. Characterisation of the Basel 1 enhanced geothermal system. *Geothermics*. 2008;37(5):469–495.
18. Kang S, Kim B, Bae S, et al. Earthquake-induced ground deformations in the low-seismicity region: a case of the 2017 M5. 4 Pohang, South Korea, earthquake. *Earthq Spectra*. 2019;35(3):1235–1260.
19. Kim B, Ji Y, Kim M, et al. Building damage caused by the 2017 M5. 4 Pohang, South Korea, earthquake, and effects of ground conditions. *J Earthq Eng*. 2022;26(6): 3054–3072.
20. McGarr A, Majer EL. The 2017 Pohang, South Korea, Mw 5.4 main shock was either natural or triggered, but not induced. *Geothermics*. 2023;107, 102612.
21. Cui P, Dang C, Zhuang J-q, et al. Landslide-dammed lake at Tangjiashan, Sichuan province, China (triggered by the Wenchuan Earthquake, May 12, 2008): risk assessment, mitigation strategy, and lessons learned. *Environ Earth Sci*. 2012;65(4): 1055–1065.
22. Cui P, Lin Y-m, Chen C. Destruction of vegetation due to geo-hazards and its environmental impacts in the Wenchuan earthquake areas. *Ecol Eng*. 2012;44:61–69.
23. Deng F, Dixon TH, Xie S. Surface deformation and induced seismicity due to fluid injection and oil and gas extraction in western Texas. *J Geophys Res Solid Earth*. 2020;125(5). n/a.
24. Li T, Cai M, Cai M. A review of mining-induced seismicity in China. *Int J Rock Mech Min Sci*. 2007;44(8):1149–1171.
25. Kang J-Q, Zhu J-B, Zhao J. A review of mechanisms of induced earthquakes: from a view of rock mechanics. *Geomechanics and Geophysics for Geo-Energy and Geo-Resources*. 2019;5(2):171–196.
26. Kneafsey TJ, Dobson P, Blankenship D, et al. An overview of the EGS Collab project: field validation of coupled process modeling of fracturing and fluid flow at the Sanford Underground Research Facility, Lead, SD. In: *43rd Workshop on Geothermal Reservoir Engineering. 2018*. 2018.
27. Ellsworth WL. Injection-induced earthquakes. *Sci Technol Humanit*. 2013;341(6142), 1225942.
28. Fan X, Scaringi G, Korup O, et al. Earthquake-induced chains of geologic hazards: patterns, mechanisms, and impacts. *Rev Geophys*. 2019;57(2):421–503.
29. Zang A, Oye V, Jousset P, et al. Analysis of induced seismicity in geothermal reservoirs–An overview. *Geothermics*. 2014;52:6–21.
30. Carpenter B, Scuderi M, Collettini C, et al. Frictional heterogeneities on carbonate-bearing normal faults: insights from the Monte Maggio Fault, Italy. *J Geophys Res Solid Earth*. 2014;119(12):9062–9076.
31. Goodfellow S, Nasseri M, Maxwell S, et al. Hydraulic fracture energy budget: insights from the laboratory. *Geophys Res Lett*. 2015;42(9):3179–3187.
32. Goodfellow SD. *Quantitative Analysis of Acoustic Emission from Rock Fracture Experiments*. University of Toronto (Canada); 2015.

33. Guglielmi Y, Cappa F, Avouac J-P, et al. Seismicity triggered by fluid injection–induced aseismic slip. *Science*. 2015;348(6240):1224–1226.
34. McGarr A, Barbour AJ. Injection-induced moment release can also be aseismic. *Geophys Res Lett*. 2018;45(11):5344–5351.
35. Segall P, Lu S. Injection-induced seismicity: poroelastic and earthquake nucleation effects. *J Geophys Res Solid Earth*. 2015;120(7):5082–5103.
36. Wu W. A review of unloading-induced fault instability. *Undergr Space*. 2021;6(5):528–538.
37. Wu W, Zhao Z, Duan K. Unloading-induced instability of a simulated granular fault and implications for excavation-induced seismicity. *Tunn Undergr Space Technol*. 2017;63:154–161.
38. Sainoki A, Mitri HS. Dynamic behaviour of mining-induced fault slip. *Int J Rock Mech Min Sci*. 2014;66:19–29.
39. Ortlepp WD, Stacey TR. Rockburst mechanisms in tunnels and shafts. *Tunn Undergr Space Technol*. 1994;9(1):59–65.
40. Sainoki A, Mitri HS. Back analysis of fault-slip in burst prone environment. *J Appl Geophys*. 2016;134:159–171.
41. Brace W, Byerlee J. Stick-slip as a mechanism for earthquakes. *Science*. 1966;153(3739):990–992.
42. Sibson R. Fault rocks and fault mechanisms. *J Geol Soc*. 1977;133(3):191–213.
43. Stesky R. Rock friction-effect of confining pressure, temperature, and pore pressure. *Rock Friction and Earthquake Prediction*. 1978:690–704.
44. Scholz CH. Earthquakes and friction laws. *Nature*. 1998;391(6662):37–42.
45. Linker M, Dieterich JH. Effects of variable normal stress on rock friction: observations and constitutive equations. *J Geophys Res Solid Earth*. 1992;97(B4):4923–4940.
46. Dou Z, Gao T, Zhao Z, et al. The role of water lubrication in critical state fault slip. *Eng Geol*. 2020;271, 105606.
47. Li J, Yuan W, Li H, et al. Study on dynamic shear deformation behaviors and test methodology of sawtooth-shaped rock joints under impact load. *Int J Rock Mech Min Sci*. 2022;158, 105210.
48. Barton N. Review of a new shear-strength criterion for rock joints. *Eng Geol*. 1973;7(4):287–332.
49. Yang ZY, Lo SC, Di CC. Reassessing the joint roughness coefficient (JRC) estimation using Z2. *Rock Mech Rock Eng*. 2001;34(3):243–251.
50. Grasselli G, Wirth J, Egger P. Quantitative three-dimensional description of a rough surface and parameter evolution with shearing. *Int J Rock Mech Min Sci*. 2002;39(6):789–800.
51. Barton N. The shear strength of rock and rock joints. *Int J Rock Mech Min Sci Geomech Abstracts*. 1976;13:255–279. Elsevier.
52. Ju Y, Wan C, Ren Z, et al. Quantification of continuous evolution of full-field stress associated with shear deformation of faults using three-dimensional printing and phase-shifting methods. *Int J Rock Mech Min Sci*. 2020;126, 104187.
53. Ju Y, Wang L, Xie H, et al. Visualization and transparentization of the structure and stress field of aggregated geomaterials through 3D printing and photoelastic techniques. *Rock Mech Rock Eng*. 2017;50:1383–1407.
54. Ju Y, Xie H, Zheng Z, et al. Visualization of the complex structure and stress field inside rock by means of 3D printing technology. *Chin Sci Bull*. 2014;59(36):5354–5365.
55. Qiu P, Yue Z, Yang R. Experimental study on mode-I and mixed-mode crack propagation under tangentially incident P waves, S waves and reflected waves in blasts. *Eng Fract Mech*. 2021;247, 107664.
56. Qiu P, Yue Z, Yang R, et al. Modified mixed-mode caustics interpretation to study a running crack subjected to obliquely incident blast stress waves. *Int J Impact Eng*. 2021;150, 103821.
57. Jaeger JC. *Elasticity, Fracture and Flow: With Engineering and Geological Applications*. Springer Science & Business Media; 2012.
58. Jaeger J. Brittle fracture of rocks. In: *ARMA US Rock Mechanics/Geomechanics Symposium*. ARMA; 1966. ARMA-66-0003.
59. Jaeger JC, Cook NG, Zimmerman R. *Fundamentals of Rock Mechanics*. John Wiley & Sons; 2009.
60. Zheng Z, Cook NG, Myer LR. Borehole breakout and stress measurements. In: *ARMA US Rock Mechanics/Geomechanics Symposium*. ARMA; 1988. ARMA-88-0471.
61. Gdoutos EE. The optical method of caustics. *Opt Laser Eng*. 2016;79:68–77.
62. Yao X, Xu W. Recent application of caustics on experimental dynamic fracture studies. *Fatig Fract Eng Mater Struct*. 2011;34(6):448–459.
63. Wang S, Li J, Li X, et al. Dynamic photoelastic experimental study on the influence of joint surface geometrical property on wave propagation and stress disturbance. *Int J Rock Mech Min Sci*. 2022;149, 104985.
64. De Barros L, Wynants-Morel N, Cappa F, et al. Migration of fluid-induced seismicity reveals the seismogenic state of faults. *J Geophys Res Solid Earth*. 2021;126(11), e2021JB022767.
65. Kisslinger C. A review of theories of mechanisms of induced seismicity. *Eng Geol*. 1976;10(2-4):85–98.
66. Segall P, Grasso JR, Mossop A. Poroelastic stressing and induced seismicity near the Lacq gas field, southwestern France. *J Geophys Res Solid Earth*. 1994;99(B8):15423–15438.
67. Abercrombie RE. Resolution and uncertainties in estimates of earthquake stress drop and energy release. *Philosophical Transactions of the Royal Society A*. 2021;379(2196), 20200131.
68. Abercrombie RE, Rice JR. Can observations of earthquake scaling constrain slip weakening? *Geophys J Int*. 2005;162(2):406–424.
69. Zhu J, Kang J, Elsworth D, et al. Controlling induced earthquake magnitude by cycled fluid injection. *Geophys Res Lett*. 2021;48(19), e2021GL092885.
70. Kisslinger C. A review of theories of mechanisms of induced seismicity. *Eng Geol*. 1976;10(2):85–98.
71. Wu H, Vilarrasa V, De Simone S, et al. Analytical solution to assess the induced seismicity potential of faults in pressurized and depleted reservoirs. *J Geophys Res Solid Earth*. 2021;126(1), e2020JB020436.
72. Shapiro SA. *Fluid-induced Seismicity*. Cambridge University Press; 2015.
73. Shapiro SA, Dinske C, Kummerow J. Probability of a given-magnitude earthquake induced by a fluid injection. *Geophys Res Lett*. 2007;34(22).
74. Yuan W, Li JC, Zou CJ, et al. A new apparatus for testing shear-slip properties of rock joint subjected to dynamic disturbance. *Exp Mech*. 2024;64(5):745–759.
75. Li B, Jiang Y, Mizokami T, et al. Anisotropic shear behavior of closely jointed rock masses. *Int J Rock Mech Min Sci*. 2014;71:258–271.
76. Homand F, Belem T, Souley M. Friction and degradation of rock joint surfaces under shear loads. *Int J Numer Anal Methods GeoMech*. 2001;25(10):973–999.
77. Barton N, Wang C, Yong R. Advances in joint roughness coefficient (JRC) and its engineering applications. *J Rock Mech Geotech Eng*. 2023;15(2):3352–3379.
78. Huan J-y, Zhang Z-q, He M-m, et al. A new statistical parameter for determining joint roughness coefficient (JRC) considering the shear direction and contribution of different protrusions. *Adv Civ Eng*. 2021;2021:1–15.
79. Yerkes RF, Ellsworth WL, Tinsley JC. Triggered reverse fault and earthquake due to crustal unloading, northwest Transverse Ranges, California. *Geology*. 1983;11(5):287–291.
80. Kwiatek G, Saarno T, Ader T, et al. Controlling fluid-induced seismicity during a 6.1-km-deep geothermal stimulation in Finland. *Sci Adv*. 2019;5(5), eaav7224.